Journal of Integrative Agriculture 2026, 25(3): 1223–1242

Available online at ScienceDirect

Journal of Integrative Agriculture



RESEARCH ARTICLE

Development of the FI-R model, a novel remote sensing method for fine-scale extraction of vegetation, using rapeseed as an example

Sixian Yin[1], Taixia Wu[1#], Shudong Wang[2], Ran Chen[1], Yingying Yang[1], Hongzhao Tang[3#]

[1] *School of Earth Sciences and Engineering, Hohai University, Nanjing 211100, China*
[2] *Aerospace Information Research Institute, Chinese Academy of Sciences, Beijing 100094, China*
[3] *Land Satellite Remote Sensing Application Center, Ministry of Natural Resources, Beijing 100048, China*

Highlights

- A novel flowering spectral index for the fine-scale extraction of angiosperms over large areas in complex multi-regional backgrounds was developed using rapeseed as an example.
- Ground hyperspectral characteristics of rapeseed and other typical crops in rapeseed planting areas were analyzed and extended to Landsat-8 imagery to develop the flowering index of rapeseed (FI-R).
- FI-R shows low sensitivity to background complexity and rapeseed varieties, and it has good applicability to multiple multi-spectral sensor images.

Abstract

The fine-scale characterization of vegetation surface information serves as a fundamental basis for studying the spatial distribution of resources and the dynamic patterns of environmental responses. Accurately extracting the distributions of different crop species is of critical importance for improving agricultural production efficiency and ensuring food security. Traditional fine-scale vegetation extraction methods often face significant challenges due to the presence of spectrally similar features and the substantial influence of background interference, which limit their applicability across large areas. As a key phenological stage of angiosperms, flowering is characterized by distinctive flowering times, floral morphology, and canopy spectral signatures, so it is an effective pathway for fine-scale vegetation extraction using remote sensing. Using rapeseed as an example, this study developed a spectral index model for precise flowering vegetation extraction (FI-R) based on Landsat OLI imagery. The model integrates a yellowness index (Blue, Green) and a peak index (Red, Nir and SWIR1) while leveraging the NDVI to mitigate background interference from spectrally similar objects. This approach successfully enables the rapid and accurate large-scale mapping of flowering vegetation under complex background conditions. The proposed method was tested in five rapeseed cultivation regions worldwide with diverse backgrounds. Validation datasets were generated using GF imagery and the U.S. CDL dataset. The FI-R model demonstrated superior capability in distinguishing flowering rapeseed from other vegetation, and achieved overall accuracies exceeding 94% in all study areas. Furthermore, FI-R is compatible with other multispectral sensors that have similar band configurations, so it is applicable to rapeseed extraction in broader contexts. The method also shows strong potential for the fine-scale extraction of other types of flowering angiosperm vegetation.

Keywords: flowering rapeseed, multispectral imagery, precise classification, spectral indices, FI-R

1. Introduction

Vegetation species exhibit varying sensitivities to climate change (Parmesan and Yohe 2003). Fine-grained vegetation classification is fundamental for assessing the potential impacts of climate on different vegetation types (Cleland *et al.* 2007). The distributional changes of individual species and the shifts in key phenological periods are regarded as fundamental for understanding the mechanisms underlying

Received 16 January 2025; Received in revised form 10 March 2025; Accepted 1 April 2025; Available online 14 May 2025
Sixian Yin, E-mail: yinsx@hhu.edu.cn; #Correspondence Taixia Wu, E-mail: wutx@hhu.edu.cn; Hongzhao Tang, E-mail: tanghz@pku.edu.cn

© 2026 CAAS. Publishing services by Elsevier B.V. on behalf of KeAi Communications Co. Ltd. This is an open access article under the CC BY-NC-ND license (http://creativecommons.org/licenses/by-nc-nd/4.0/). Peer review under responsibility of Editorial Board of *Journal of Integrative Agriculture*.
doi: 10.1016/j.jia.2025.05.006

ecosystem functions and responses to environmental change, thereby assisting decision-makers in formulating effective strategies for ecological protection and adaptation. Remote sensing technology has the advantages of extensive spatial coverage, rapid data acquisition, high spatiotemporal resolution, and integrative capabilities, so it has become an indispensable tool for precise vegetation monitoring and management (Ienco *et al.* 2019; Lyu *et al.* 2020; Weiss *et al.* 2020).

Fine-scale vegetation extraction methods in remote sensing can be broadly categorized into two main approaches. The first approach is based on feature-driven artificial intelligence techniques. Algorithms such as support vector machines (SVM), random forests (RF), and deep learning methods (Timm and McGarigal 2012; Song *et al.* 2020; Yan *et al.* 2021; Pandey and Jain 2022) can achieve high classification accuracy in small regions. However, their performance is often constrained by factors such as sample quality, sensor parameters, radiative transfer processes, and underlying surface backgrounds. These limitations make it challenging to generalize trained models to other images or regions (Weiss *et al.* 2020). The second approach involves vegetation index-based models, which enable the rapid acquisition of fine-scale vegetation distribution information over large areas. Existing indices, such as the normalized difference vegetation index (NDVI) (Freden *et al.* 1974), enhanced vegetation index (EVI) (Huete *et al.* 2002), and normalized difference yellowness index (NDYI) (Sulik and Long 2016), are widely used in vegetation mapping (Gao *et al.* 2020). However, these indices lack the specificity needed for accurately extracting individual vegetation types.

To address this limitation, researchers have developed spectral indices tailored to specific vegetation types. For instance, Cao *et al.* (2020) proposed the wide dynamic range vegetation index (WDRVI) for monitoring sugar beet growth, while Ribeiro *et al.* (2023) created various vegetation indices to track lettuce growth stages, and Vásquez *et al.* (2023) constructed a new vegetation index using the cyan, orange, and near infrared (NIR) bands to analyze soybean growth dynamics. Despite these advancements, the current modeling approaches still face several challenges. For example, some fine-scale vegetation extraction models account for only a limited range of land cover types, leading to high false-positive rates and significant overgeneralization. The enhanced mangrove vegetation index (EMVI) proposed by Yang *et al.* (2022) demonstrates good adaptability in the coastal areas of China but fails to adequately account for and differentiate wetland vegetation with spectral characteristics similar to mangroves. In addition, certain fine-scale vegetation indices rely on multi-temporal imagery, which carries a high risk of data gaps. For instance, Ashourloo *et al.* (2019) relied on significant increases in the red and green bands over two periods to identify the flowering phase of rapeseed. However, obtaining two high-quality consecutive scenes is often difficult due to cloud cover. Finally, many fine-scale vegetation extraction indices have been developed for specific study areas, but their applicability to other regions remains uncertain. Further validation is required to assess their effectiveness across diverse environments.

In terms of imagery selection, hyperspectral imagery is commonly used for fine-scale interspecies vegetation extraction at small spatial scales due to its higher spectral resolution, which provides richer information (Szantoi *et al.* 2013; Wu *et al.* 2017; Yan *et al.* 2019; Zhang *et al.* 2019; Sun *et al.* 2021; Nuijten *et al.* 2024). For instance, Chen *et al.* (2009) employed hyperspectral data and a spectral mixture model to develop a flowering coverage index for *Halerpestes tricuspis* in alpine meadows on the Tibetan Plateau. Similarly, Wouters *et al.* (2013) used hyperspectral data to identify characteristic bands for determining the spatial abundance and distribution of pear flower buds. Yao *et al.* (2023) integrated hyperspectral imagery with flower indices, random forests, and stepwise multiple linear regression (SMLR) models to estimate flowering intensity in rice fields. However, the application of hyperspectral imagery at larger scales is severely limited by its limited data availability and poor spatial coverage. Previous studies relying on hyperspectral imagery for fine-scale vegetation extraction faced challenges such as limited spatial coverage and insufficient data density, which preclude large-scale application. Moreover, many research areas are relatively small and lack representativeness, while the models used often consider only a narrow range of land cover types. This results in issues such as spectral overgeneralization, high false-positive rates, and multi-response phenomena. Addressing these challenges requires identifying an alternative approach that can overcome the constraints of hyperspectral data while ensuring robust and accurate vegetation extraction at larger spatial scales.

The flowering period is a distinct phase within the phenological cycle of vegetation, and a key stage that exhibits high sensitivity to climate change. The diversity of flowers among angiosperms is primarily manifested in three aspects: flowering time, flower color, and floral morphology. Differences in flowering time are primarily influenced by temperature, photoperiod and vernalization effects. Driven by their reproductive strategies, different plant species bloom at varying times to align with pollinator activity periods and minimize interspecific competition. Flower color is largely determined by pigments and environmental factors. Flowering plants use flowers with vibrant colors to attract pollinators (Narbona *et al.* 2021), and the presence of pigments such as carotenoids and anthocyanins significantly alters the spectral characteristics of flowering vegetation canopies (Asen 1975). On the other hand, floral morphology evolves under the influences of genetic factors and ecological adaptation needs, leading to diverse structures and arrangements of floral organs. During the flowering phase, the canopy spectral signature of a plant differs significantly from those of its pre- and post-flowering phenological stages. Furthermore, spectral responses during flowering vary across plant species. The timing of flowering is driven by differences in photoperiod, and it introduces temporal spectral distinctions that can allow remote sensing to differentiate between species with similar flower colors and morphologies. Consequently, the flowering phase serves as an effective window for precise vegetation identification using spectral characteristics. Some studies have focused on vegetation extraction during the flowering phase. For example, Sulik

and Long (2015) developed the rapeseed yellowness index (RYI) based on ground-based hyperspectral data, which was later expanded to NDYI (Sulik and Long 2016). Similarly, Chen *et al*. (2019) proposed the enhanced bloom index (EBI) to monitor the flowering dynamics of apricot trees, and demonstrated its robustness across multiple scales and using data from various multispectral satellite platforms.

Among the numerous flowering plants, rapeseed (*Brassica napus* L.) is extensively cultivated as a key economic crop in various regions worldwide. Its blooming period is marked by conspicuously bright yellow flowers, and is regarded as the optimal stage for remote sensing monitoring and yield estimation throughout the growing season (Zhang and Flottmann 2018). Variations in cultivation practices across different rapeseed-growing regions can affect the accuracy of spectral models. This is particularly evident in China, where the agricultural landscape is fragmented due to the predominance of smallholder farming, thereby increasing spatial heterogeneity in crop remote sensing mapping (Yu *et al*. 2018). Research into the typical growth cycle and physiological characteristics of rapeseed is expected to enhance the precision of vegetation classification and to offer novel insights for the refined classification of complex vegetation types.

Medium- to high-resolution multispectral imagery, such as Landsat, has been widely used for fine-scale vegetation extraction over large areas due to its abundant data availability, long time series, and strong surface coverage capabilities (Szantoi *et al.* 2013; Liu *et al.* 2020; Tian *et al.* 2022; Zhang *et al.* 2023; Chen *et al.* 2024). Utilizing Landsat OLI imagery, this study aims to: (1) analyze hyperspectral canopy data of flowering vegetation during the flowering phase to identify effective spectral features, and (2) develop a high-precision vegetation extraction model for complex backgrounds based on flowering-phase characteristics. To achieve these objectives, rapeseed was chosen as a case study. We constructed the flowering-phase rapeseed index (FI-R) and conducted three experiments to validate the effectiveness of this method: (1) The performance of FI-R, existing vegetation indices, RF, and SVM methods in distinguishing rapeseed from other vegetation and yellow-colored objects was compared; (2) the extraction results of rapeseed using FI-R under diverse backgrounds were evaluated and they were compared with models that excluded the shortwave infrared (SWIR) bands; (3) the applicability of FI-R was tested across other multispectral imagery datasets.

2. Materials and methods

2.1. Study areas

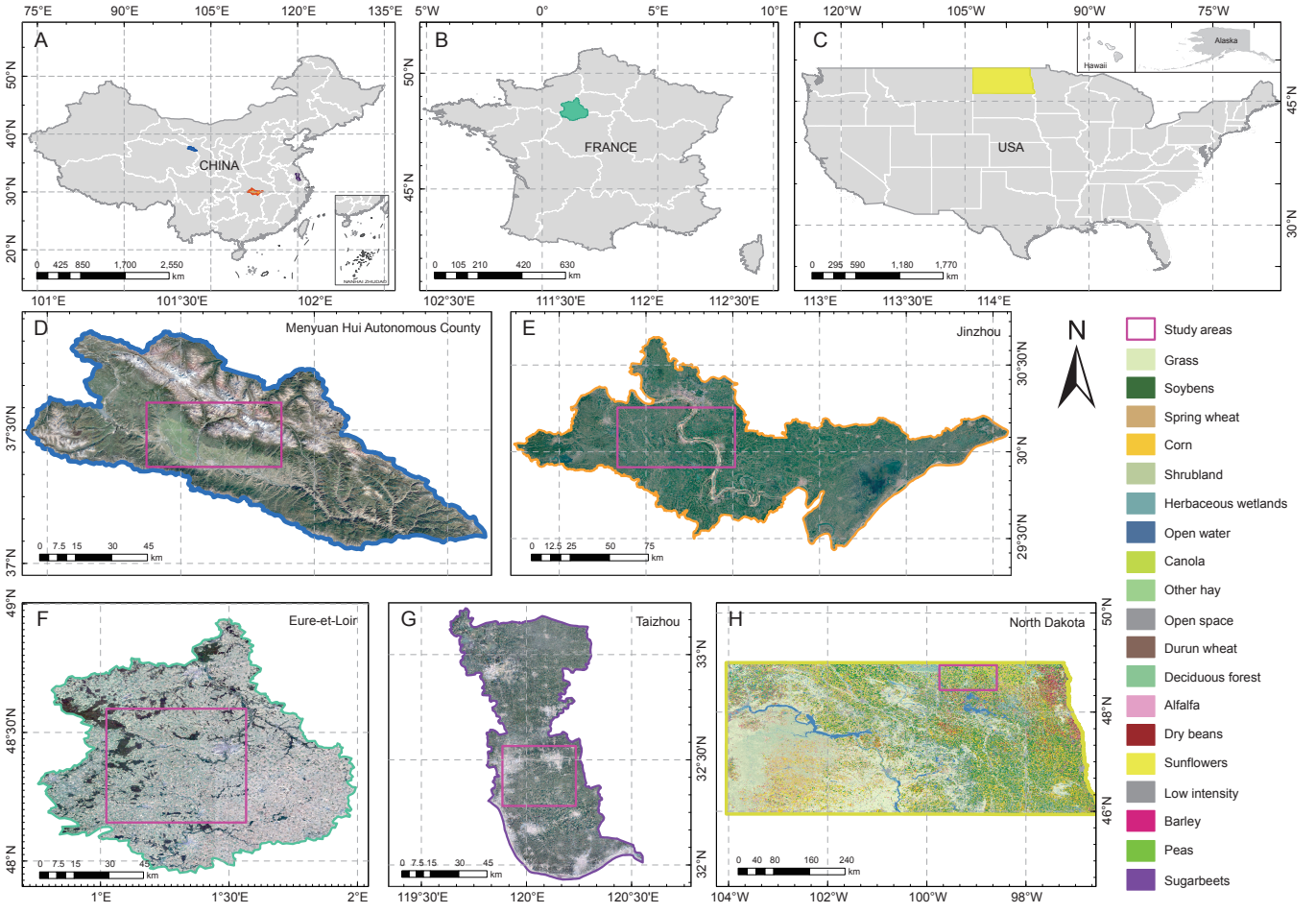
This study selected three primary study areas and two validation areas (Fig. 1) which encompass a variety of climatic conditions, including plateau continental, subtropical monsoon, temperate maritime, and continental climates. These sites also range from large-scale single-crop farming to fragmented planting in complex backgrounds. The main study areas are in Menyuan Hui Autonomous County, Qinghai, China (site A), Jingzhou City, Hubei Province, China (site B), and Eure-et-Loir Department, France (site C). In China, the rapeseed planting areas are divided into two major ecological regions based on climate and cultivation type: spring rapeseed and winter rapeseed. Winter rapeseed is primarily found in the Yangtze River basin, and accounts for 80% of rapeseed cultivation in China. Conversely, spring rapeseed is predominantly cultivated in the western China region, with significant plantings in Qinghai and Inner Mongolia. This study designated site A as the research area for spring rapeseed and site B for winter rapeseed, with site C selected as an additional research area. Beyond these three locations, the study also included Taizhou in Jiangsu Province, China (site D), and North Dakota, USA (site E) as evaluation and validation areas for the model.

Site A is located in Menyuan Hui Autonomous County in northeastern Qinghai Province, China (37°05′15′′–37°52′41′′N, 100°55′30′′–102°38′16′′E), and covers an area of approximately 6,896 km². This area experiences a plateau continental climate with an annual average temperature of 1.5°C and average annual precipitation of 517.6 mm. The unique ecological environment of this region fosters the growth of northern spring rapeseed, which is adapted to cool, moist conditions and has strong cold resistance. The effective accumulated temperature required from sowing to harvest is only 1,500°C, which is half that required by other rapeseed varieties (Meng *et al.* 2023). Menyuan County is recognized as the origin of northern spring rapeseed in China, with the rapeseed flowering period occurring in July each year.

Site B is located in Jingzhou City, Hubei Province, in the heart of the Jianghan Plain, China (29°54′39′′–30°15′15′′N, 111°50′06′′–112°30′40′′E), and covers an area of approximately 2,888.23 km². The Jianghan Plain is an important grain-producing area in China, with the cultivation of rice, cotton, rapeseed, wheat, and soybeans. Land scarcity and population pressure have led to a high degree of fragmentation in agricultural lands and dispersed planting patterns of rapeseed. The flowering period of rapeseed occurs annually from March to early April.

Site C (48°8′59′′–48°35′33′′N, 1°13′43′′–1°33′59′′E) covers an area of approximately 1,982.94 km² and is located in the Eure-et-Loir department of France. This department is France's largest grain-producing area, with the cultivation of crops such as wheat, rapeseed, and peas. Wheat occupies 40% of the agricultural land area, while rapeseed production is also among the highest in the country. The flowering period of rapeseed occurs annually from late March to early May.

Site D covers an area of approximately 5,787.36 km² (331°55′46′′–33°13′03′′N,119°37′43′′–120°33′09′′E) and is located in Xinghua, a county-level city under the jurisdiction of Taizhou City in Jiangsu Province, China. The cultivated land area is large, but the degree of fragmentation is high. The rape field with the style of Thousand Islands has become the most famous tourist attraction in the local area. The rape in this area is mainly distributed in the scenic spot, and some rape is also scattered outside the scenic spot. The main crops cultivated in this region include wheat, rice, corn, and rapeseed. The flowering period of rapeseed occurs annually from March to May. This location allowed for an assessment



审图号：GS 京 (2026) 0069 号

Fig. 1 Geographic locations of the five study areas. A–C show the study sites within their respective countries. D, E, and G correspond to the Chinese study sites. F shows the French study site C in the Eure-et-Loir Department. H shows the USA study site E in North Dakota, together with the cropland data layer (CDL).

of the model's ability to precisely extract rapeseed in areas with high degrees of farmland fragmentation.

Site E is located in North Dakota, USA (48°26′06′′–48°59′31′′N, 98°34′45′′–99°45′46′′W), and covers an area of approximately 5,241.26 km². The flowering period of rapeseed occurs annually in July. According to the agricultural land data layer (https://nassgeodata.gmu.edu/CropScape/), the primary crops cultivated in this region include corn, soybeans, rapeseed, sunflowers, and wheat, and it provides a mapping of the distributions of these crops. This location allowed for the verification and evaluation of the model's ability to extract rapeseed among multiple crop types.

2.2. Research data and pre-processing

Imagery data The Landsat continuous mission was initiated in 1972 and has provided over 50 years of ground monitoring data, making it one of the most valuable datasets for studying the Earth's surface (Kennedy *et al.* 2014). Landsat-8 has served as part of the continuous Earth observation data collection mission since 2013, and it offers a spatial resolution of 30 m and a temporal resolution of 16 d. All cloud-free images of Landsat-8 OLI L2C2 during the flowering period were obtained from the Google Earth Engine (GEE) platform (https://code.earthengine.google.com/). GEE is a free global-scale data processing platform that encompasses worldwide data analysis capabilities and a vast collection of satellite imagery datasets, including Landsat-8 data (Gorelick *et al.* 2017).

As the data source for this study, Landsat-8 imagery consists of five visible light bands, two NIR bands, and two SWIR bands acquired by the OLI sensor, with a spectral range from 0.433 to 12.51 μm. The Landsat Collection2 Level2 data obtained from GEE were subjected to atmospheric correction, which was built upon the higher geometric correction and radiometric calibration accuracy of the Level 1 data.

For validating the research results in this study, high-resolution Gaofen (GF) data, particularly PMS images with high spatial resolution, served as the primary reference. In areas where high-resolution GF data were unavailable, Sentinel-2 images were used as supplementary reference data for validation. Geometric correction was applied to both GF-1 and GF-2 data, followed by the fusion of panchromatic and multispectral bands, resulting in

GF-1 data with a resolution of 2 m and GF-2 data with a resolution of 0.8 m. Visual interpretation was then employed to obtain accurate samples of rapeseed and other land cover distributions. This process ensured a more precise assessment of the distribution patterns of rapeseed and other features through visual interpretation of the merged high-resolution GF data.

Since the rapeseed flowering period (Fig. 2) coincides with increased rainfall, we manually filtered out ineffective images with significant cloud cover based on rapeseed phenology and visual interpretation. Specific Landsat-8 images were selected for site A (July 12, 2018), site B (March 22, 2021), site C (April 27, 2021), site D (March 26, 2021), and site E (July 23, 2021), each corresponding to the peak flowering period or close to it. The optical image dates and distributions for all five study areas are detailed in Table 1.

Ground hyperspectral data The hyperspectral data at the canopy scale were measured using an ASD FieldSpec 4 Pro spectrometer (Analytical Spectral Devices, Inc., Boulder, CO, USA) during the flowering period on 7 and 12, March 2022. The spectral range of the spectrometer was between 350 and 2,500 nm, with 3 and 8 nm spectral resolution in the 350–1,000 and 1,000–2,500 nm regions, respectively (Zheng *et al.* 2018). All canopy spectral measurements were taken with a 25° field of view at a height of 1.4 m above the ground. A calibration panel was performed every five measurements to correct for changes in the illumination conditions. All experiments were measured under cloudless conditions with favorable visibility between 10:00 a.m. and 2:00 p.m. (UTC+8) when minimum variations in the solar view angle occurred. Each measurement represented an average of 10 data collection points so these were considered as the reflectance spectra of the samples. In total, 52 samples were collected, including 20 rapeseed flower canopy samples. Positions of the spectra near 1,400 and 1,900 nm were removed

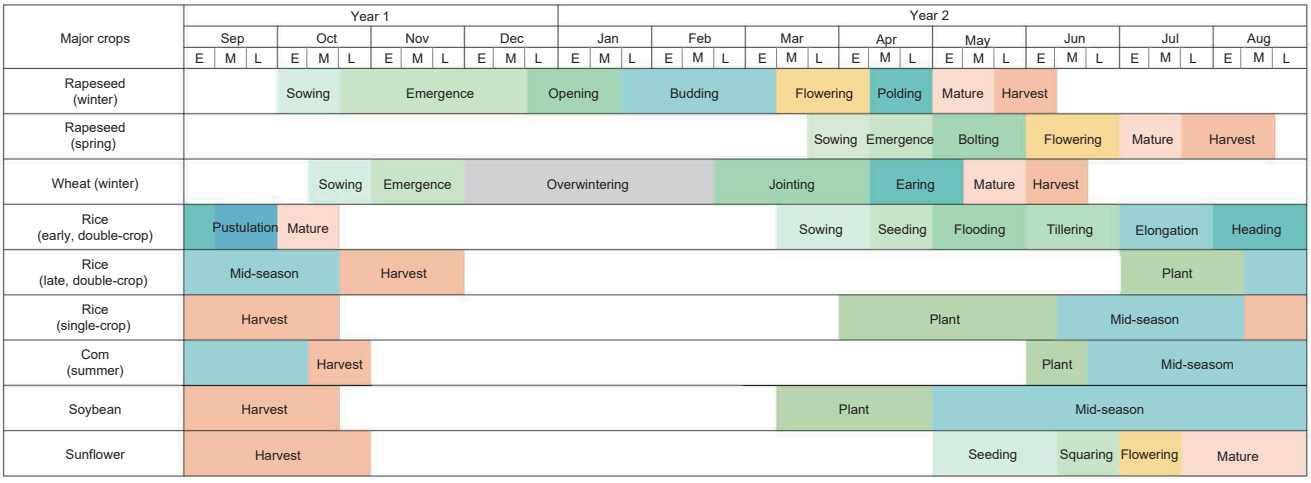


Fig. 2 The phenological periods of major crops in the five study areas. 'E', 'M' and 'L' represent the first, middle and last ten days of the month, respectively.

Table 1 Optical imaging information used in this study

Location	Sensor	Acquisition date (mon/d/yr)	Sensor	Acquisition date (mon/d/yr)
Site A	Landsat-8 (30 m)	12/7/2018	MODIS (500 m)	26/7/2018
		12/7/2018	Sentinel-2 (10 m)	23/7/2020
	GF-2 (0.8 m)	26/7/2018		
Site B	Landsat-8 (30 m)	22/3/2022	MODIS (500 m)	28/3/2022
	GF-2 (0.8 m)	3/15/2022	Sentinel-2 (10 m)	28/3/2020
		3/15/2022		
		3/20/2022		
Site C	Landsat-8 (30 m)	27/4/2021		
	Sentinel-2 (10 m)	23/4/2021		
		25/4/2021		
Site D	Landsat-8 (30 m)	26/3/2021		
		12/7/2021		
	GF-2 (0.8 m)	24/3/2021		
Site E	Landsat-8 (30 m)	23/7/2021	MODIS (500 m)	18/7/2021
		7/23/2021	Sentinel-2 (10 m)	24/7/2021

because of noise. The research flowchart is shown in Fig. 3.

2.3. Canopy spectral characteristics of flowering rapeseed

In the visible spectrum, pigments are the primary factors influencing the spectral responses of vegetation, with chlorophyll, carotenoids, and anthocyanins playing dominant roles (Wong 2023). In the NIR region, the spectral characteristics of vegetation are primarily determined by leaf internal structure and dry matter content. In the SWIR region, water absorption exerts a strong influence on the vegetation spectral response, although leaf structure and dry matter content also contribute to some extent.

We randomly collected approximately 50 sets of data and calculated the average spectral curves for six land cover types: rapeseed flowers, rapeseed flowering canopies, other tree canopies, grasslands, soil, and wheat canopies (Fig. 4). These spectral curves were analyzed to identify

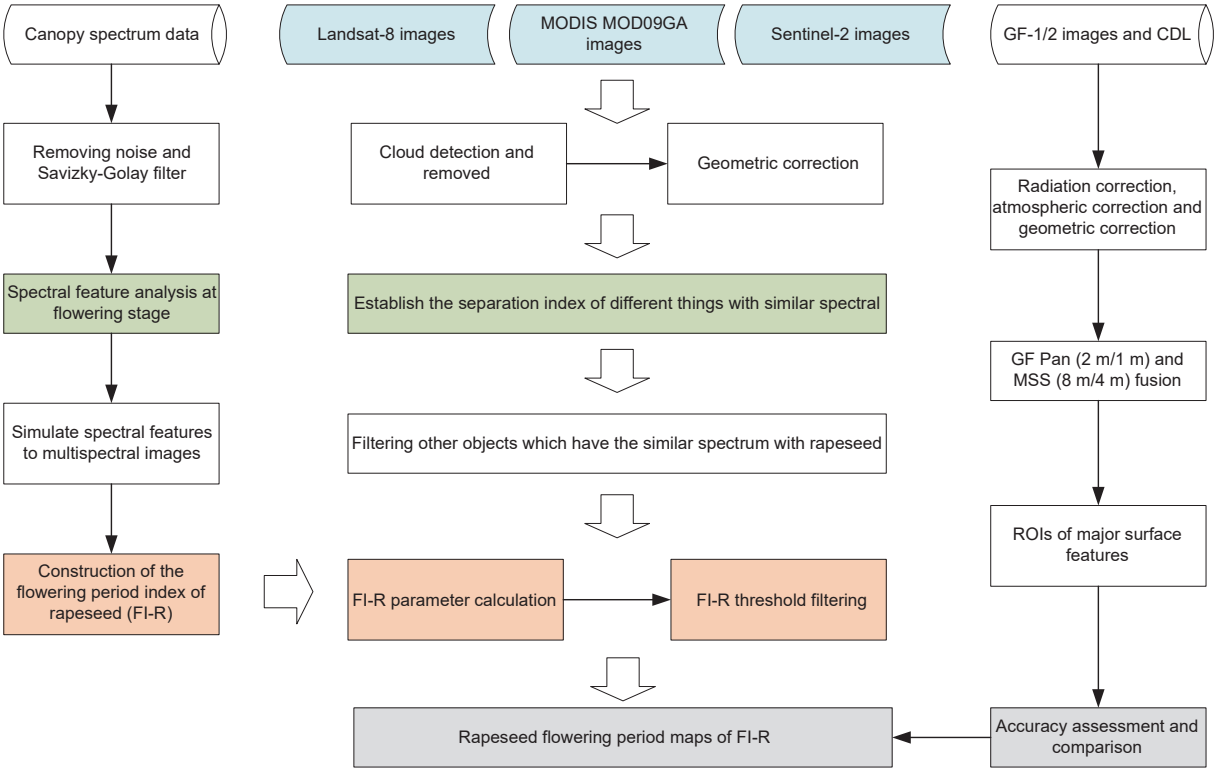


Fig. 3 Flowchart for the precise identification of flowering rapeseed.

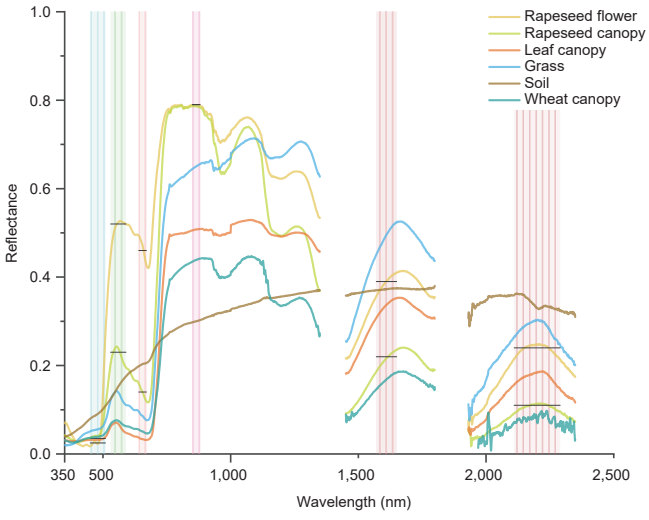


Fig. 4 Overlay of the hyperspectral curves of typical features within the subsurface of the oilseed rape growing area with Landsat-8 bands. The transparent colored stripes indicate the Landsat-8 band widths and the short horizontal lines indicate the corresponding Landsat band values for the oilseed rape and wheat spectra.

suitable spectral bands for constructing the FI-R index. Taking rapeseed as an example, its growth cycle generally includes three distinct canopy structures: The first stage, encompassing the seedling and bud-stem elongation phases, is dominated by green foliage; the second stage, corresponding to the flowering phase, is characterized by a canopy dominated by yellow petals (or occasionally white or other colors), interspersed with green leaves; and the third stage, or maturity phase, features a canopy primarily composed of green pods and stems (Sulik and Long 2016). These three canopy structures exhibit significant differences in their interception of solar radiation, with the flowering phase showing the most distinct changes in spectral absorption and reflection.

During the bud stage, all primary stem leaves emerge, followed by the gradual unfolding of the inflorescences. The flowers turn yellow under the influence of carotenoids and flavonoids (Grotewold 2006; Zhang *et al.* 2015), which absorb a significant amount of blue light in the visible spectrum, particularly within the 400–500 nm range. As the yellow flowers become more prevalent in the canopy, they overshadow a large number of the green leaves, which reduces the canopy's ability to absorb red light from the sun, enhances its capacity to reflect green light, and slightly increases its absorption of blue light. Consequently, the difference in reflectance between the blue and green bands becomes more pronounced, so the ratio of green to blue reflectance is employed as an index of yellowness. This is reflected in the common normalized vegetation indices, with the NDVI value gradually decreasing from the bud stage to the flowering period and reaching its lowest point during peak bloom (Shen *et al.* 2009). Conversely, the NDYI value gradually increases, also peaking during the flowering stage.

The canopy spectrum of flowering rapeseed is a mixture of yellow flower and green leaf spectra. It exhibits strong reflectance in the red and NIR bands, with particularly high

values in the NIR band compared to other land cover types. A notable spectral peak occurs between the red and SWIR bands, where the reflectance values are nearly equivalent. These three features approximate an isosceles triangle, and the difference between the NIR peak and the mean reflectance of the red and SWIR bands is notably large. The NIR band is commonly regarded as a characteristic band for vegetation due to the influences of internal leaf structure and pigments, leading to pronounced reflectance. During the flowering phase, rapeseed retains this characteristic, with its NIR reflectance values notably higher than those of non-vegetation land covers. Furthermore, the dense and multi-layered arrangement of rapeseed flowers and leaves enhances NIR reflectance, resulting in values that exceed those of other vegetation types. In the SWIR band, rapeseed canopy reflectance during the flowering phase is higher than in the pre-flowering phase. SWIR values increase with the flower coverage rate, so it is a useful indicator of flowering intensity. In typical rapeseed planting environments — which are dominated by farmland, urban areas, and other background elements — soil, buildings, and water bodies are the primary non-vegetation background features. These elements generally exhibit higher SWIR reflectance than rapeseed canopies. To reduce the influence of background features such as soil, buildings, and water, the SWIR band around 1,600 nm was selected as a characteristic wavelength for distinguishing rapeseed from non-living background land covers.

In summary, the unique spectral characteristics of the rapeseed canopy are exploited by this model. The marked blue light absorption by yellow flowers, coupled with variations in canopy green reflectance, accentuates the yellowness feature in the green-to-blue ratio and distinguishes it from other yellow vegetation. Furthermore, the reflectance in the red, NIR, and SWIR bands approximate an isosceles triangle, with the NIR peak being particularly prominent, thereby reducing interference from non-biological yellow elements. In addition, the SWIR band is employed to mitigate background interference from soil and water. The blue and green bands serve as indices for yellowness, while the red, NIR, and SWIR bands function as indices for peak values. Rapeseed can be identified and extracted by leveraging these two characteristic features of the flowering canopy.

2.4. Background simplification

Previous studies (Meng *et al.* 2020) have reported that the accurate extraction of winter rapeseed is often hindered by the phenomenon of "spectral similarity with different objects," primarily winter wheat. As shown in Fig. 2, winter rapeseed and winter wheat have similar phenological cycles, with both being sown in October and harvested the following June. Furthermore, Fig. 4 demonstrates that their spectral curves exhibit similar trends, reflecting the characteristic of "spectral similarity with different objects". During most phenological stages, distinguishing winter rapeseed from winter wheat based on spectral signals alone is challenging. However, winter rapeseed enters its flowering phase in March and April, during which the yellow flowers alter the spectral signature of the canopy. These changes are particularly pronounced in the red, green, blue, and NIR bands. Due to the significant variations in these bands, vegetation indices can be used to distinguish winter rapeseed from winter wheat during the flowering phase.

Samples of flowering rapeseed, bare soil, non-flowering rapeseed, wheat, and other photosynthetic vegetation were selected from the Landsat-8 imagery of site B on March 22, 2021. At least 2,000 pure pixel samples for each type of ground object were selected and verified with higher-resolution satellite imagery to validate the distribution areas of each ground object type.

The reflectance, color differences, and values of NDVI and NDYI for full-blossom rapeseed, bare soil, non-full blossom rapeseed, other photosynthetic vegetation, and wheat were compared. Fig. 5-A shows an optical image of site B (March 20, 2020, GF-2), while Fig. 5-B–F display field images of full-blossom rapeseed, bare soil, non-full blossom rapeseed, other photosynthetic vegetation, and wheat, respectively. The average spectral trends of non-full blossom rapeseed, wheat, and other photosynthetic vegetation are similar, with high reflectance values in the green and red bands causing the rapeseed flowers to appear bright yellow. Therefore, during the full-blossom period, rapeseed has higher values in the visible part of the spectrum compared to the other three types of ground cover. A lesser increase in the NIR band relative to the red band indicates a decreasing trend in the NDVI values for winter rapeseed during this stage. At that time, winter wheat is transitioning from reviving and turning green to the standing and jointing period, with the leaves gradually lengthening as the plant shifts from prostrate to upright growth. These changes increase the vegetation cover and, consequently, the NDVI values. As an index of yellowness, NDYI effectively highlights the bright yellow characteristic of flowering rapeseed but cannot distinguish between non-full blossom rapeseed, wheat, and other crops.

During this critical phenological period, based on the opposing trends in NDVI values between winter wheat and winter rapeseed, and the relatively high NDVI values of winter wheat among these classes, an NDVI threshold segmentation was used to mask the winter wheat. A total of 2,478 winter wheat samples, 1,242 flowering rapeseed samples, and 792 non-flowering rapeseed samples were selected for a significant statistical analysis of their NDVI values. The model aims to precisely identify the distribution areas of rapeseed, including during the key phenological period of flowering for both full blossom and non-full blossom rapeseed. To minimize the impact of winter wheat on the model's extraction capabilities and enhance the accuracy of identifying winter rapeseed, statistical data were used to determine an NDVI threshold for masking the ground objects similar to winter rapeseed, primarily winter wheat.

2.5. Model construction

The analysis of the ground-based hyperspectral characteristics of rapeseed canopies during the flowering phase in Section 2.3 demonstrated that the spectral features in the blue, green, red, NIR, and SWIR bands exhibit significant changes during the transition from the pre-flowering to flowering phases. Among these features, the

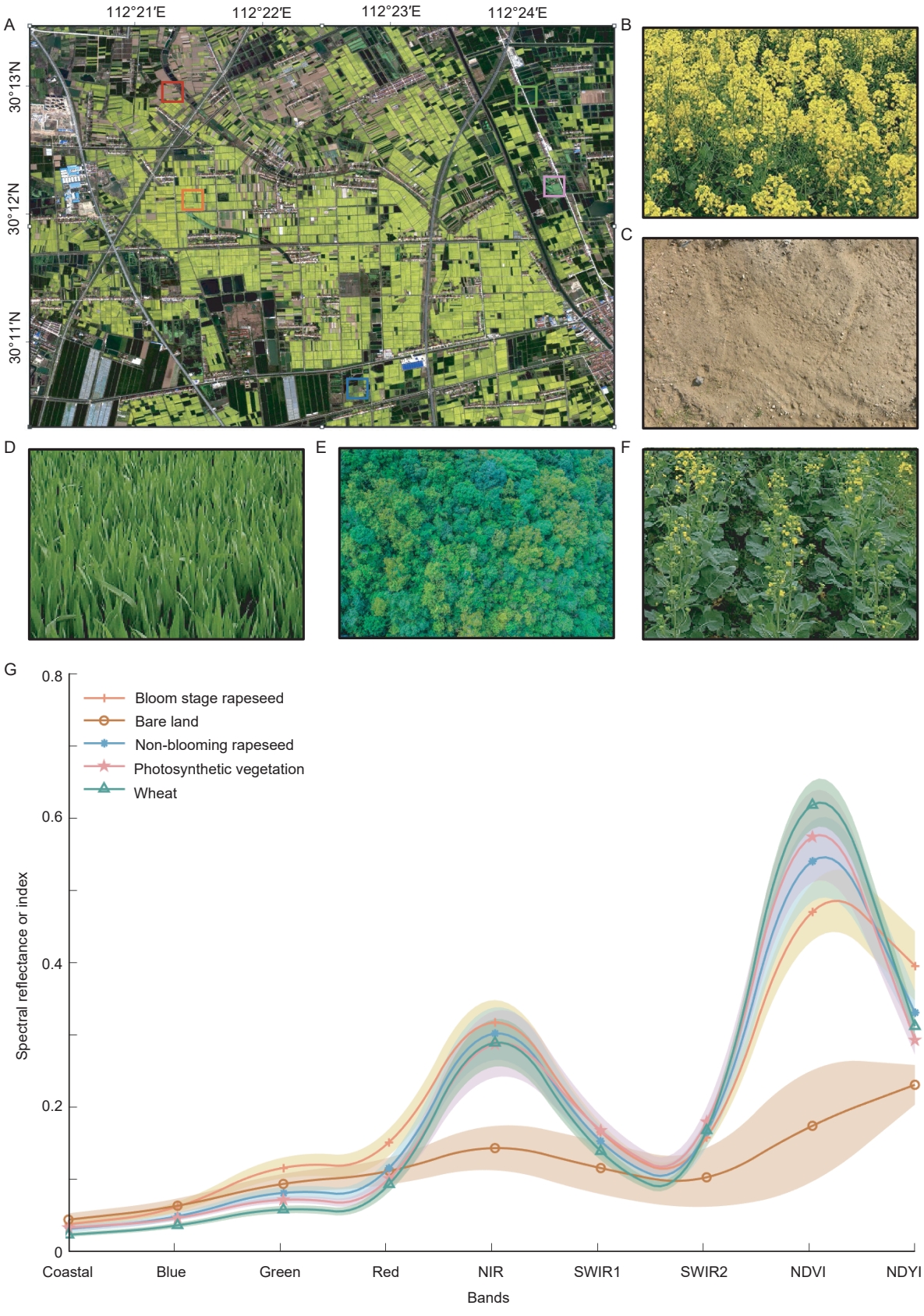


Fig. 5 Comparison of rapeseed with other typical underlying surface features at different flowering levels. A, GF-2 image (RGB) at site B during the flowering stage on 15 March 2022. B, field image of rapeseed at the full flowering stage. C, photo of bare soil on farmland. D, field image of rapeseed at the beginning of the flowering stage. E, live image of sub-bedding vegetation. F, field image of winter wheat during the flowering period of rapeseed. G, typical sub-bedding type Landsat-8 bands and the NDVI and NDYI profiles. NIR, near infrared; SWIR, short-wave infrared; NDVI, normalized difference vegetation index; NDYI, normalized difference yellowness index.

slope from the blue to green bands serves as an indicator of the yellowness of rapeseed canopies, while the red, NIR, and SWIR bands represent peak indicators. Using these findings, the following rapeseed flowering phase extraction model, FI-R, was developed as described by the following equation:

$$FI\text{–}R=\left(\frac{\rho_{Green}}{\rho_{Blue}}\right)^{m}\times(\rho_{NIR}-n\times\rho_{Red}-n\times\rho_{SWIR}) \quad (1)$$

where ρ_{Green}, ρ_{Blue}, ρ_{NIR}, ρ_{Red}, and ρ_{SWIR} correspond to the reflectance values from Landsat-8 bands 2 (Blue), 3 (Green), 4 (Red), 5 (NIR), and 6 (SWIR), respectively. The proposed FI-R model is designed to amplify the characteristic signals of rapeseed during its flowering period, ensuring that the FI-R values for rapeseed pixels significantly exceed those of other ground objects. In the formula, *m* represents an adjustment factor, and *n* is a feature factor. The proposed FI-R model is designed to amplify the characteristic signals of rapeseed during its flowering phase, emphasizing the high reflectance of densely packed yellow flowers. Notably, the reflectance of rapeseed in the NIR band is typically greater than 1.5 times the sum of its reflectance in the red and SWIR bands. Therefore, the part $\rho_{NIR}-n\times\rho_{Red}-\rho_{SWIR}$ was structured to ensure that the FI-R values for rapeseed are generally positive. A higher FI-R value indicates a higher probability that the corresponding pixel represents rapeseed flowers.

2.6. Parameterization method

The canopy spectrum of flowering rapeseed exhibits a characteristic red-edge phenomenon, with a sharp increase in reflectance from the red band to the NIR band, which is typical of vegetation. However, the dense flowers and multiple reflections within the canopy cause the NIR reflectance of flowering rapeseed to reach the highest value among typical land cover types. In the SWIR band, the reflectance of rapeseed flowers is relatively high and exceeds that of background soil. However, the overall SWIR reflectance of rapeseed canopies drops sharply and becomes comparable to red band reflectance. Notably, the mean reflectance values of both the red and SWIR bands for flowering rapeseed canopies are among the lowest among the sampled land cover types.

Using these characteristics, parameter *n* was introduced to adjust the magnitude of the differences between the NIR, red, and SWIR bands. This adjustment enhances the "isosceles triangle" peak feature of flowering rapeseed, where the NIR, red, and SWIR bands form a nearly symmetrical peak, while ensuring that the FI-R values for rapeseed pixels remain positive. The parameter *m* serves to amplify the rapeseed flower signal while reducing the influence of background information. By minimizing the variability caused by differences in background types, *m* helps to mitigate the uncertainties associated with diverse land cover backgrounds. Furthermore, adjusting *m* balances the weights of the two spectral features, allowing the characteristics of flowering rapeseed to become more prominent. Simulation experiments determined the effective range for *m* values to be [0, 8], with an increment of 0.5 used for testing.

In eqs. (2)–(4), C represents the comparison of the performance of rapeseed against other valuable background objects within the FI-R model.

$$C(B|NB)=|\bar{B}-\overline{NB}| \quad (2)$$

$$C(B|W)=|\bar{B}-\overline{W}| \quad (3)$$

$$C(B|PV)=|\bar{B}-\overline{PV}| \quad (4)$$

where $\bar{B}$ represents the average FI-R of the rapeseed flowering area in the Landsat-8 imagery of site B, $\overline{NB}$ is the average FI-R of the non-flowering rapeseed area within the same image, $\overline{W}$ is the average FI-R of the wheat planting area in the image, and $\overline{PV}$ is the average FI-R of randomly sampled photosynthetic vegetation within the image. A larger C value indicates a greater difference in the comparison parameter within the model. The distribution areas of the ground objects listed above were verified using high-resolution satellite imagery (i.e., GF1/2). Based on the classification results from the Landsat-8 imagery, uniform sampling was conducted for each type of ground object, and the average model value was calculated for each ground object type.

To facilitate the analysis, the C values were normalized to fall within the (0, 1) interval. C_{max} is defined as the maximum value of C for each formula:

$$ND(B|NB)=C(B|NB)/C_{max} \quad (5)$$

$$ND(B|W)=C(B|W)/C_{max} \quad (6)$$

$$ND(B|PV)=C(B|PV)/C_{max} \quad (7)$$

The normalized values of C(B|NB), C(B|W) and C(B|PV) are represented as ND(B|NB), ND(B|W), ND(B|PV), respectively. The *m* value that shows the best performance for flowering rapeseed within ND was selected as the modulation factor.

2.7. Accuracy evaluation

Overall accuracy (OA), producer's accuracy (PA), user's accuracy (UA), Precision, Recall, and the F1-score were used to evaluate the performance of the FI-R model in rapeseed mapping. Accuracy reflects the ratio of correctly classified samples to the total number of samples. However, in cases of imbalanced samples, such as when the proportion of rapeseed planting in the study area is excessively low or high, this metric may not effectively evaluate performance. Hence, the F1-score was used to supplement the assessment of model performance under such circumstances. The F1-score, composed of Precision and Recall, represents the probability of correctly predicted samples among all samples predicted to be correct (Precision), and the probability of samples predicted to be correct among all actual correct samples (Recall). Precision and Recall often exhibit opposite trends at the same classification confidence level. The F1-score considers both factors in a weighted average manner. Under conditions of sample imbalance, the F1-score is known to be more robust than OA because it effectively balances the impacts of both false negatives and false positives. By combining accuracy and the F1-score, we could accurately assess the extraction effectiveness of the FI-R model across different research areas and various proportions of rapeseed cultivation area.

$$Precison=\frac{TP}{TP+FP} \quad (8)$$

$$Recall=\frac{TP}{TP+FN} \quad (9)$$

$$F1=\beta\times\frac{Precision\times Recall}{Precision+Recall} \quad (10)$$

Based on these evaluation metrics, four different rapeseed mapping index models were compared with the rapeseed distributions at three locations (sites A, D, and E) obtained from higher-resolution imagery and ground reference data. The four models were an extraction model based on NDYI (Sulik and Long 2015), an extraction model based on WRI (Zhang *et al.* 2022), an extraction model based on CI (Zamani-Noor and Feistkorn 2022), and an extraction model based on CFI (Tian *et al.* 2022). In addition, two machine learning methods, RF and SVM, were used to extract the rapeseed distribution. The validation point dataset was selected as shown in Fig. 6.

$$NDYI=\frac{Green-Blue}{Green+Blue} \quad (11)$$

$$WRI=\frac{NIR-Green}{NIR+Green}\times\frac{Blue}{Green+Red} \quad (12)$$

$$Rapeseed=WRI_{bf}-WRI_{f}>0$$

$$CI=NIR\times(Red+Green) \quad (13)$$

$$CFI=\frac{NIR-Red}{NIR+Red}\times(Red+2\times Green-Blue) \quad (14)$$

where Red, Green, Blue, and NIR correspond to the red, green, blue, and near-infrared spectral bands, respectively. WRI_{bf} represents the WRI imagery before the flowering phase, while WRI_{f} denotes the WRI imagery during the flowering phase.

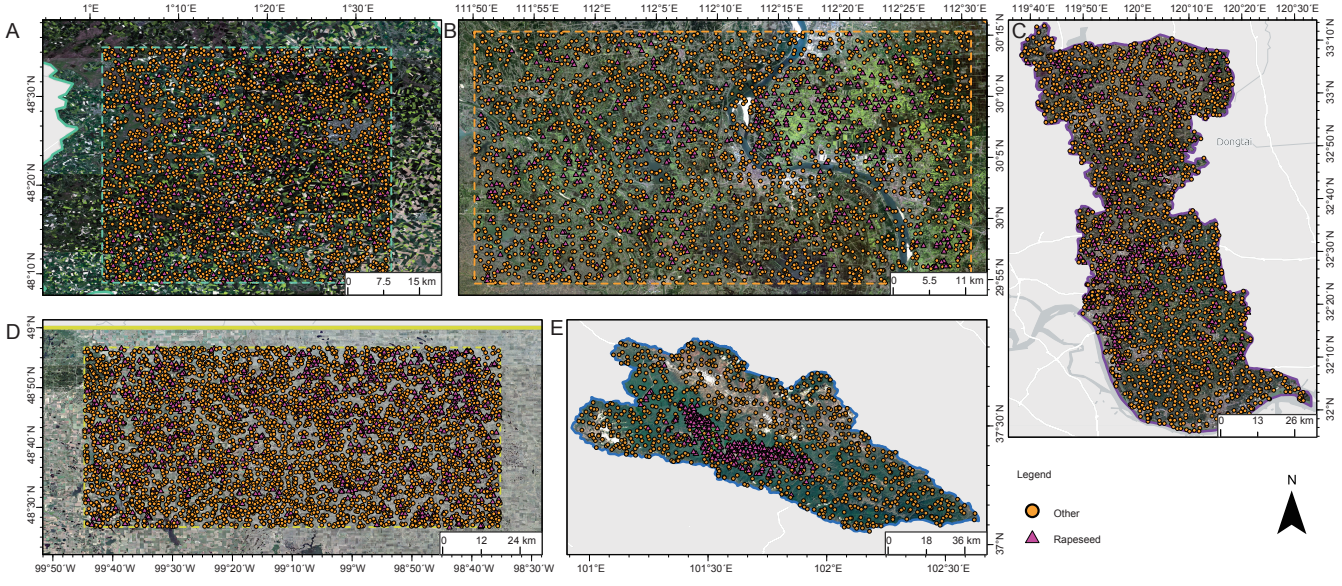
3. Results

3.1. Background simplification performance

An analysis of the NDVI for flowering rapeseed and winter wheat at site B (Fig. 7) identified an NDVI background simplification threshold of 0.64. This threshold was then used to minimize interference from spectrally similar background features, which were dominated by winter wheat. The effectiveness of this threshold was further verified by applying a wheat mask to evaluate the performance of the FI-R model for site B. To achieve this, multispectral and panchromatic imagery were fused using the nearest neighbor decision (NND) method, which produced GF-2 imagery with a spatial resolution of 1 m. Using the high-resolution GF-2 imagery, a total of 11,493 FI-R values were collected for flowering rapeseed, winter wheat, and other land cover types. Before applying the winter wheat mask, the FI-R model achieved an overall accuracy of 82.79% and an F1-score of 0.36 for site B. After masking out winter wheat, the FI-R model's overall accuracy improved significantly to 95.64% and the F1-score increased to 0.91. These results demonstrate a substantial improvement in accuracy following the application of the wheat mask.

To ensure that the masking threshold for wheat applies not only to specific regions but is also suitable for most areas where winter rapeseed and winter wheat are cultivated together, the wheat masking method was also validated using data from site D. Before applying the wheat mask, the overall accuracy of the FI-R model extraction at site D was 76.35%, with an F1-score of 0.29. After masking, the overall accuracy of the FI-R estimation model increased to 98.40%, with the F1-score rising to 0.95.

These results indicate that during the flowering period of rapeseed, there is a significant difference in the NDVI values between winter rapeseed and winter wheat. Accounting for this difference can greatly reduce the impact of spectrally similar winter wheat on the FI-R model's ability to extract winter rapeseed (Fig. 8).



审图号：GS 京 (2026) 0069 号

Fig. 6 The distributions of sample points and true-color Landsat OLI imagery for the study areas. A, Eure-et-Loir, France (Date: 2021-4-4). B, Jingzhou, Hubei Province, China (Date: 2021-3-22). C, Taizhou, Jiangsu Province, China (Date: 2021-3-26). D, North Dakota, United States (Date: 2021-7-23). E, Menyuan Hui Autonomous County, Qinghai Province, China (Date: 2018-7-12).

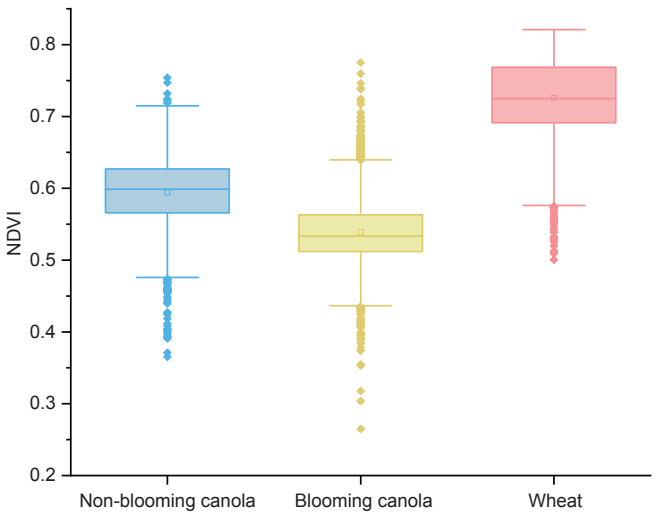
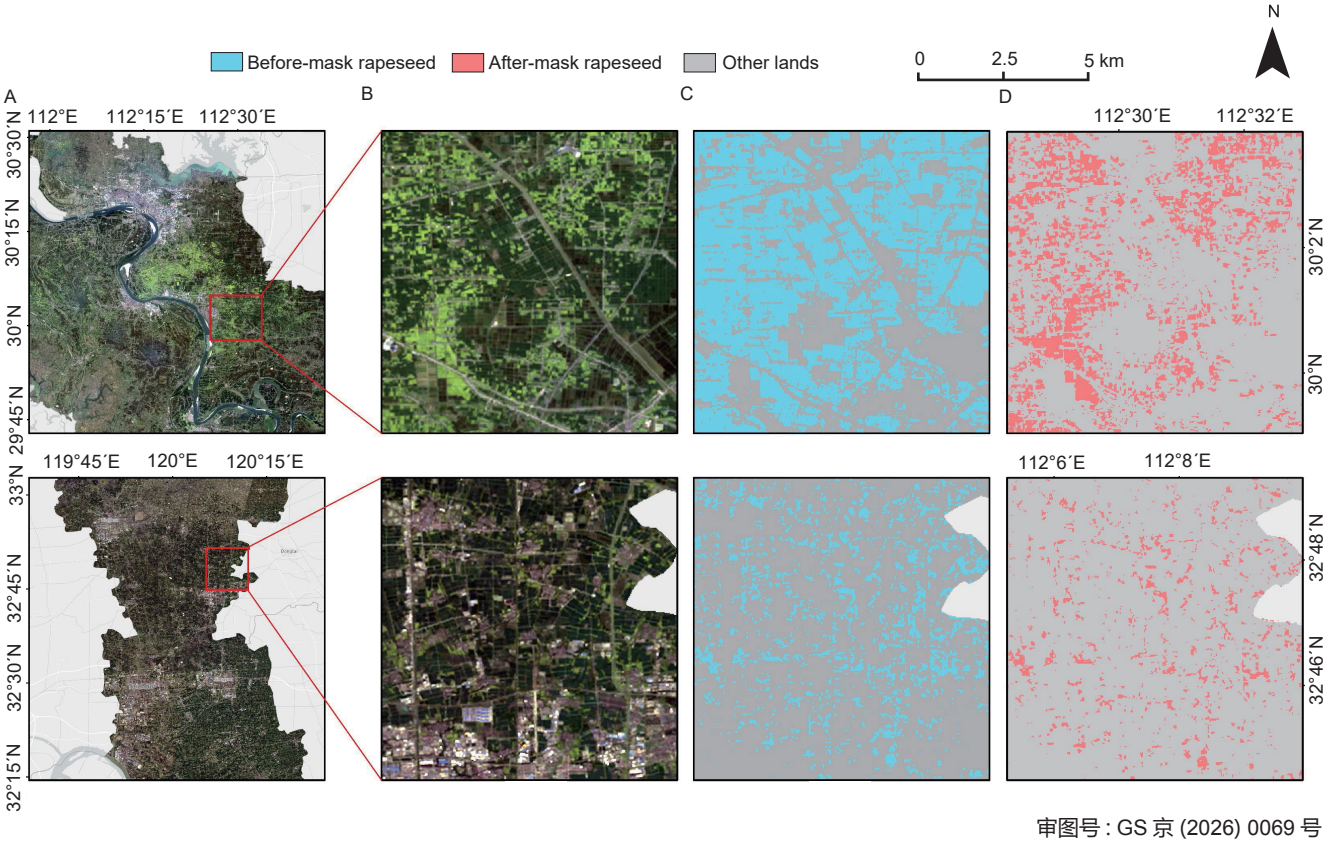


Fig. 7 Significant differences in the normalized difference vegetation index (NDVI) values of full blossom rapeseed, non-full blossom rapeseed, and winter wheat image elements.

3.2. Model parameter determination

In eq. (1), the parameter *n* is a feature factor that not only reflects the spectral reflectance distribution of rapeseed during the flowering stage in the red, NIR, and SWIR1 bands but also mathematically characterizes the triangular shape formed by the data from these three bands. Specifically, the reflectance values of the red, NIR, and SWIR1 bands can be sequentially connected in two-dimensional space to form a triangle, with the near-infrared reflectance positioned at the vertex and the red and SWIR1 reflectance values determining the endpoints of the base. The distance from the NIR vertex to the midpoint of the base can be calculated and then normalized by the average reflectance of the base endpoints to define the parameter *n*. When *n* attains a value of 0.5, it indicates that the resulting triangle is approximately isosceles in shape, with the base endpoints exhibiting similar reflectance values while the NIR reflectance is markedly higher, thereby producing a prominent peak feature. From a geometric perspective, as the triangle approaches an isosceles shape, the midline distance increases, suggesting that, under typical background conditions, rapeseed in its flowering stage demonstrates elevated reflectance in the NIR band. Thus, by assigning equal weights to the red and SWIR1 bands and using their average reflectance as a baseline, the influence of anomalous or noisy data in a single band is effectively mitigated. Furthermore, the normalized *n* value not only encapsulates the high-peak spectral characteristic of flowering rapeseed but also maintains robust stability and comparability. This design ensures that the NIR peak is not unduly affected by extreme values in either of the side bands, thereby demonstrating resistance to outliers and robustness in data processing. In addition, after



审图号：GS 京 (2026) 0069 号

Fig. 8 Comparison of FI-R model flowering rapeseed extraction before and after wheat masking in site B and site E. A, locations of the site B and site E study areas. B, local zoomed-in views of the study areas. C, FI-R model rapeseed extraction results before unmasking. D, FI-R model rapeseed extraction results after wheat masking.

normalizing the reflectance data for each band to account for potential interferences from atmospheric conditions, moisture, and a soil background, the parameter *n* more accurately captures the spectral variation trends of rapeseed during flowering and remains comparable across different samples. Mathematically, this normalization method renders *n* as a smooth function with low sensitivity to minor reflectance fluctuations, thereby exhibiting excellent noise resistance in the statistical analyses.

The parameter *m* is a modulation factor used to adjust the balance between yellowness features and peak features, thereby reducing the probable impact of similar ground objects on the model. By calculating the average values of $\overline{B}$, $\overline{NB}$, $\overline{W}$, and $\overline{PV}$ in site B using Landsat-8 imagery, the range of *m* values was set from 1 to 8, with increments of 0.5. The integer part from 1 to 7 was selected for sample calculations. For different *m* values, the FI-R values and C values for each type of ground object were calculated, as shown in Table 2. In addition, for convenient comparison, these metrics were normalized to calculate ND(B|NB), ND(B|W), and ND(B|PV), as shown in Table 3. The ND value ranges over (–1, 1), where an ND value close to 0 indicates lower distinguishability between two types of ground objects, and an ND value close to 1 or –1 indicates complete distinguishability. As shown in Fig. 9, with an increase in the *m* value, the three ND curves gradually converge to a stable value. When *m*=2.5, the distinguishability between flowering and non-flowering rapeseed begins to decrease, and the distinguishability between flowering rapeseed and other photosynthetic vegetation reaches saturation. Comparing different *m* values, the distinguishability between flowering rapeseed and wheat is greater than that between flowering and non-flowering rapeseed at *m*=6, effectively compressing the potentially confusing ground objects and enhancing the identification signal of flowering rapeseed.

Table 2 Comparison of C values for different *m*-values of FI-R for a typical understory

C	FI-R-1 (*m*=1)	FI-R-2 (*m*=2)	FI-R-3 (*m*=3)	FI-R-4 (*m*=4)	FI-R-5 (*m*=5)	FI-R-6 (*m*=6)	FI-R-7 (*m*=7)
$\overline{B}$	0.5805	1.3797	3.3124	8.0274	19.6232	48.3527	120.0155
$\overline{NB}$	0.3847	0.7753	1.5700	3.1939	6.5283	13.4069	27.6647
$\overline{W}$	0.5156	0.9846	1.8824	3.6037	6.9077	13.2580	25.4793
$\overline{PV}$	0.4355	0.8030	1.4830	2.7430	5.0811	9.4263	17.5123
C(B|NB)	**0.1959**	**0.6044**	1.7425	4.8335	13.0949	34.9457	92.3508
C(B|W)	0.0649	0.3952	1.4300	4.4237	12.7155	35.0947	94.5362
C(B|PV)	0.1450	0.5767	**1.8294**	**5.2845**	**14.5421**	**38.9264**	**102.5032**

Bold numbers are the maximum C values for each *m*-value.

Table 3 Comparison of FI-R values with different *m*-value normalized C values for a typical sub-surface

(/Cmax)	FI-R-1 /0.1959	FI-R-2 /0.6044	FI-R-3 /1.8294	FI-R-4 /5.2845	FI-R-5 /14.5421	FI-R-6 /38.9264	FI-R-7 /102.5032
ND(B|NB)	1	1	0.9525	0.9147	0.9005	0.8977	0.9010
ND(B|W)	0.3316	0.6538	0.7816	0.8371	0.8744	0.9016	0.9223
ND(B|PV)	0.7404	0.9542	1	1	1	1	1.0000

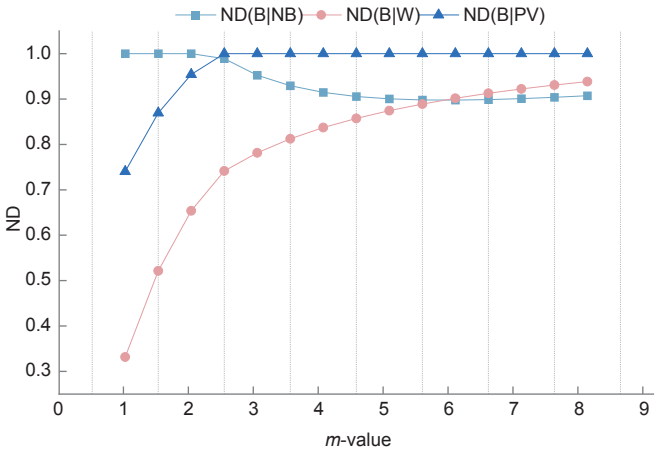


Fig. 9 Comparison of interclass normalized difference (ND) values for the FI-R model for rapeseed based on different values of *m*.

3.3. Spatial distributions of rapeseed at sites A, B, and C

Based on the parameter analysis in Section 2.4 and parameter determination in Section 3.2, the FI-R model was finalized in the form of eq. (15) .

$$FI\text{–}R=\left(\frac{\rho_{Green}}{\rho_{Blue}}\right)^{6}\times(\rho_{NIR}-0.5\times\rho_{Red}-0.5\times\rho_{SWIR}) \quad (15)$$

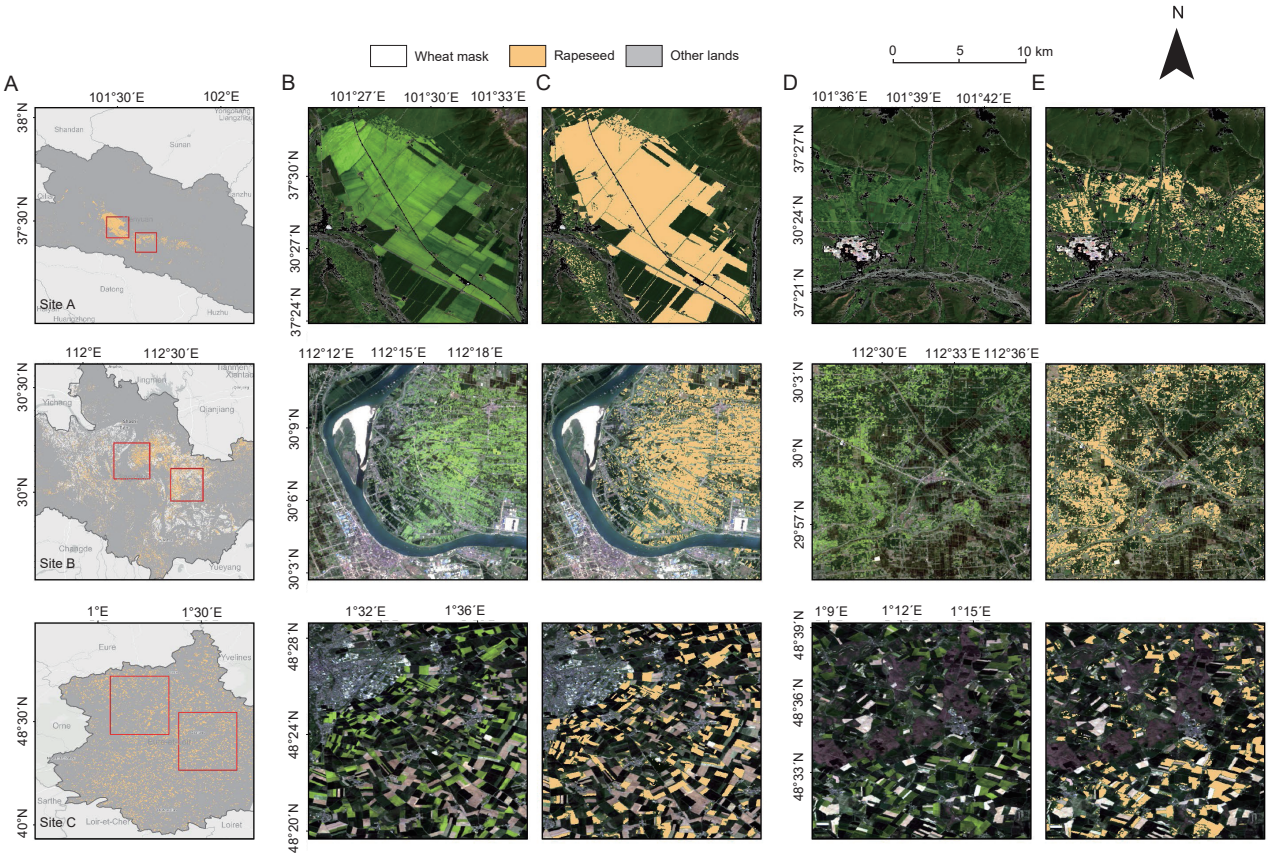
Using this model, the flowering-phase rapeseed distribution was extracted for sites A, B, and C. Fig. 10-A illustrates the overall extent of winter rapeseed cultivation in the three study areas, with detailed enlarged views of the red rectangles provided in Fig. 10-B–E. Note that Fig. 10-B and D show the optical imagery, while Fig. 10-C and E display the extracted winter rapeseed areas, which correspond one-to-one with the optical imagery. In site B, where both winter wheat and winter rapeseed are cultivated, the extraction results for winter rapeseed — after applying a winter wheat mask — align well with the optical satellite imagery, as do the results for sites

A and C. The detailed enlarged views reveal that variations in flowering degree among different field blocks are obvious in site A, which is characterized by a single agricultural background and extensive planting areas. The FI-R model can effectively extract rapeseed pixels corresponding to varying flowering stages with clearly defined boundaries. In site B, the more intensive rapeseed planting pattern and smaller field plots result in numerous mixed pixels. Although the FI-R model adequately identifies rapeseed pixels on this fragmented land, it does not fully recognize certain mixed pixels associated with areas of lower planting density or during the late flowering stage. In site C, the FI-R model effectively extracts rapeseed pixels from fields with uniform planting density, irrespective of whether the background is urban or agricultural. For these three distinct planting densities and backgrounds, non-rapeseed land cover types such as impermeable surfaces, forests, buildings, water bodies, and other croplands were effectively excluded. In addition, both the light green pre-flowering rapeseed and the bright yellow flowering-phase rapeseed were successfully extracted.

3.4. Accuracy evaluations and model comparison

Using higher-resolution imagery, sample libraries for rapeseed and other land cover types were established for sites A–D (Fig. 6). For site E, the rapeseed validation dataset was created using the U.S. CDL dataset. These datasets were used to validate the accuracy of rapeseed extraction using the FI-R model. In sites B and D, the background was already adjusted to remove the impact of winter wheat, while in the other sites, the FI-R model was applied directly, with model threshold values chosen based on the FI-R pixel values of the lower blossom rapeseed content. Note that even the less-flowering rapeseed pixel FI-R values are higher than the FI-R values of most of the remaining ground features. The accuracy validation results indicated that the overall accuracy in each research area exceeded 96%, and the F1-score values were above 85%. Therefore, the FI-R model effectively mitigates the impact of spectrally similar non-rapeseed objects in the background and accurately extracts flowering rapeseed across diverse background conditions by leveraging the two key spectral features of flowering-phase rapeseed. The validation results of the rapeseed flowering index model's extraction accuracy across the five study areas are shown in Table 4.

Fig. 11 presents a visual comparison between the five rapeseed mapping methods listed and two machine learning methods in Section 2.7 across sites A, D, and E. The threshold for the WRI method was set to 0, as recommended in the corresponding paper, while the thresholds for the other methods were determined based on the values of the same pixel with lower degrees of rapeseed flowering across the



审图号：GS 京 (2026) 0069 号

Fig. 10 Spatial distribution of rapeseed. A, general situation of rapeseed cultivation in the three study areas. B and D, views of the true-color optical images for 12 July, 2018, 22 March, 2022 and 27 April, 2021, respectively. C and E, superimposed views of the rapeseed cultivation distribution maps associated with the satellite images for B and D.

Table 4 Validation of the extraction accuracy of the rapeseed flowering index model for the five study areas

Study area	Overall accuracy (%)	Precision (%)	Recall (%)	F1-score (%)
Site A (Menyuan)	97.74	92.06	97.33	94.62
Site B (Jinzhou)	98.40	97.40	93.30	95.30
Site C (Eure-et-Loir)	96.13	83.22	90.07	86.51
Site D (Taizhou)	96.84	82.09	97.06	88.95
Site E (North Dakota)	96.21	77.48	94.80	85.87

different methods. Both the SVM and RF methods were trained using the same training set, and all the methods were validated against the same validation set.

In site A, rapeseed is primarily cultivated in large central plots with a scattered distribution along the edges. In areas with simple backgrounds and low landscape fragmentation, most rapeseed indices perform well. However, the NDYI and CI methods exhibit over-extraction issues, mistakenly identifying parts of green vegetation under a mountain shadow influence as rapeseed. On the other hand, the WRI model could not find usable pre-flowering imagery for the same rapeseed growing cycle, limiting its application. Both

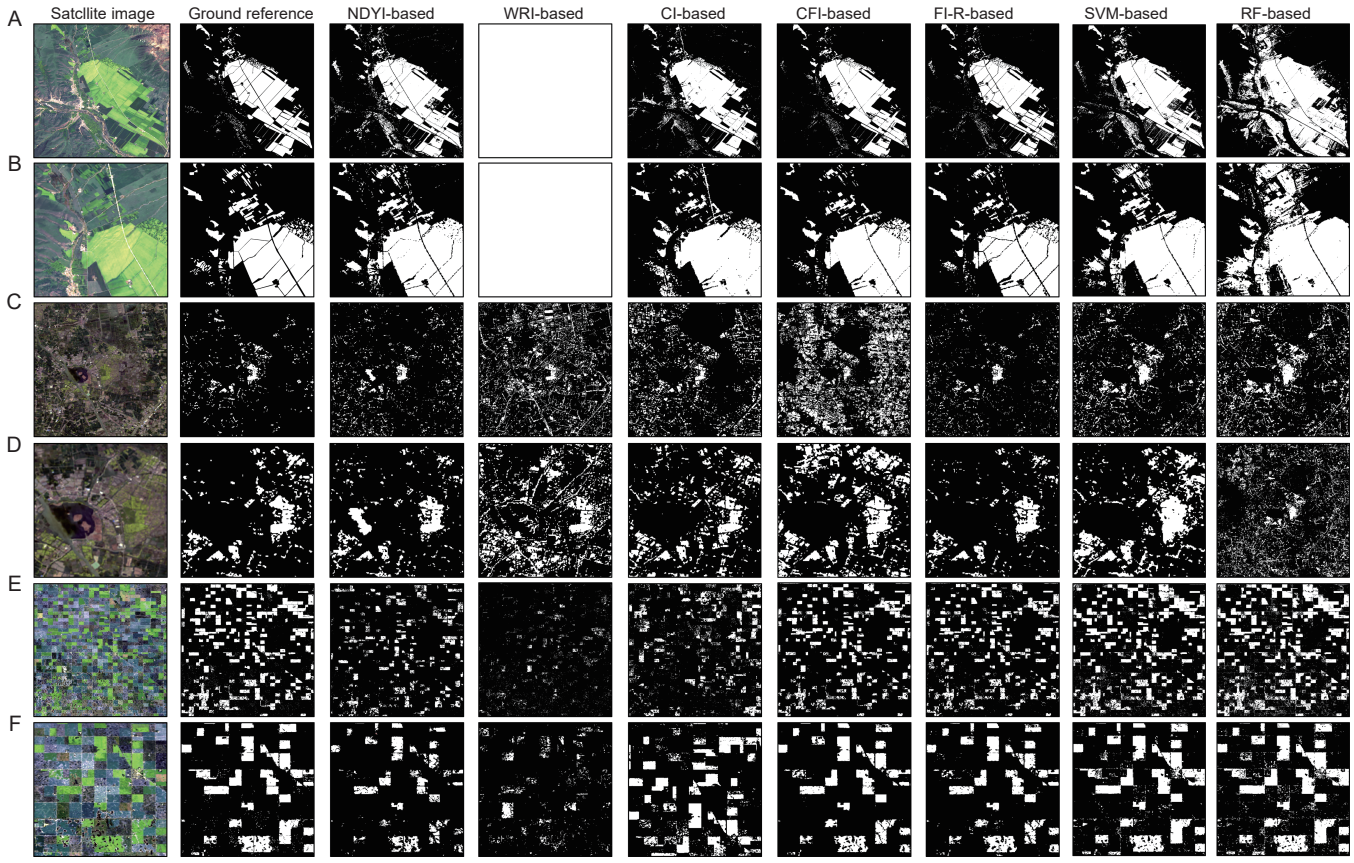


Fig. 11 Visual comparison of the five rapeseed index methods and two machine learning methods. A, C, and E, visual effects of rapeseed extraction for site A, site D, and site E, respectively. B, D, and F, local zoom-in effects for site A, site D, and site E, respectively.

the SVM and RF models demonstrated over-extraction problems, with RF misclassifying many other crop pixels compared to SVM. Furthermore, both models incorrectly identified mixed pixels as rapeseed, such as those from field ridges.

In site D, the FI-R model performed significantly better than the other methods. This study area is characterized by extensive winter wheat cultivation, a dispersed rapeseed planting pattern, and a complex ground background. The NDYI method was able to extract most rapeseed pixels but showed some omission errors, while the presence of winter wheat had only a minimal impact on its performance. Conversely, the CI and CFI methods were sensitive to winter wheat, resulting in varying degrees of over-extraction. Furthermore, the CI method incorrectly identified vegetation pixels in water bodies. The WRI method erroneously extracted roads and other background features, and its performance was similarly influenced by the presence of winter wheat. The non-flowering imagery for this area was taken on January 14 and February 22, 2021, so the reliance of WRI on specific phenological periods was a limitation. Both the SVM and RF methods showed issues of over-extraction and omission errors during initial training. In particular, the RF-based method suffered from severe salt-and-pepper noise under complex backgrounds, and failed to accurately identify flowering rapeseed patches.

In site E, the FI-R model also outperformed the other methods. This area is characterized by a complex background comprising both farmland and wetlands, with rapeseed co-cultivated alongside other crops. The NDYI and WRI methods showed some omission errors compared to the CDL ground reference dataset. Since the WRI method relies on time-series imagery, it was sensitive to deviations in the selection of specific phenological periods, which limited its regional applicability to areas dominated by winter rapeseed. The non-flowering imagery for this site was taken on July 23, 2021. The CI method exhibited significant over-extraction issues, while both the CFI and FI-R models performed well, showing minimal salt-and-pepper noise and fewer misclassifications. The SVM and RF methods also performed relatively well in this area. The structured nature of large-scale farmland and distinct crop types allowed the machine learning methods to effectively capture and identify the flowering rapeseed features.

As shown in Table 5, the FI-R model demonstrated the best overall accuracy and F1-score. The CFI method performed well in other areas but showed significant errors when winter wheat was present, with numerous misclassified winter wheat pixels. The CI method exhibited instability among the different regions, and frequently over-extracted non-rapeseed features. The NDYI method could effectively extract rapeseed distribution without being affected by winter wheat but consistently showed omission errors. While the WRI method was suitable for extracting winter rapeseed, it had strict requirements for non-flowering imagery timing. Therefore, differences between non-flowering and flowering imagery led to high uncertainty in the rapeseed distribution results. Both the SVM and RF machine learning methods rely heavily on training datasets, so they require extensive improvements in training to perform well under complex surface backgrounds. In comparison to these approaches, the FI-R model demonstrated a superior ability to distinguish flowering rapeseed from other land cover types. It consistently performed well across various backgrounds, climates, and levels of landscape fragmentation. The thresholds for rapeseed pixel identification were well-defined and showed substantial differentiation from other land cover types.

Table 5 Accuracy validation of the five rapeseed extraction indices for the site A, site D and site E extraction results

Study area	Method	Overall accuracy (%)	Precision (%)	Recall (%)	F1-score (%)
Site A (Menyuan)	NDYI	97.43	98.19	90.97	94.44%
	WRI	–	–	–	–
	CI	94.01	90.25	83.33	86.66
	CFI	97.90	92.78	97.35	95.01
	FI-R	97.74	92.06	97.33	94.62
	SVM	98.29	97.83	94.42	96.10
	RF	95.95	98.19	85.27	91.28
Site D (Taizhou)	NDYI	91.60	91.04	66.79	77.05
	WRI	86.04	83.58	53.25	65.05
	CI	82.46	89.30	46.56	61.21
	CFI	71.55	96.75	34.86	51.26
	FI-R	96.84	82.09	97.06	88.95
	SVM	86.62	95.52	53.86	68.88
	RF	85.89	94.77	52.48	67.55
Site E (North Dakota)	NDYI	93.21	56.39	95.75	70.98
	WRI	82.89	10.56	28.15	15.35
	CI	92.94	75.83	76.15	75.99
	CFI	97.31	84.58	96.67	90.22
	FI-R	96.21	77.48	94.80	85.87
	SVM	97.78	96.25	89.42	92.71
	RF	93.73	96.39	71.18	81.89

4. Discussion

4.1. Resistance of FI-R to remaining features

The ratio of green to blue bands effectively captures the variation in the quantity of yellow rapeseed flowers, which serves as a key indicator for the changes in yellowness (Sulik and Long 2016). In the background of rapeseed cultivation, there are also various other yellow feature objects, such as sunflowers, ginkgo trees, yellow buildings, and other yellow flowers. The ability of the FI-R model to discriminate yellow features approximating rapeseed was tested by field sampling the hyperspectral data of these features as well as Landsat-8 image spectral features (Table 6). Ground hyperspectral data for flowering rapeseed, winter jasmine, and pansies (yellow) were measured on the same day and averaged over ten measurements. Rapeseed, yellow buildings, ginkgo trees, and sunflowers were identified with the aid of higher-resolution imagery to obtain their pure pixel spectral values in the Landsat-8 images. As shown in Fig. 12, rapeseed exhibits the highest NIR values and the steepest slope in the blue-green bands among these four types of objects. The red band and SWIR1 band values for rapeseed are lower than those of the other objects. This distinction highlights the unique spectral signature of rapeseed, which aids in its identification and differentiation from other yellow objects in the landscape (Fu *et al.* 2024b).

The FI-R model values derived from ground-based hyperspectral simulations for rapeseed, winter jasmine, and yellow pansies exhibit strong separability. The notably higher FI-R values for yellow pansies compared to flowering rapeseed can be attributed to the higher coverage area of yellow flowers in artificially cultivated environments and the higher yellowness of the flowers relative to rapeseed blossoms. However, due to their natural distribution and ornamental characteristics, yellow pansies do not interfere with the extraction of flowering rapeseed in agricultural settings. FI-R performs well in the pure yellow vegetation pixels, and flowering rapeseed is also highly separable from the typical widely distributed yellow vegetation such as ginkgo and sunflower, in addition to having different flowering phenological periods. These yellow structures also do not affect rapeseed identification because their FI-R values are much smaller than the FI-R values of oilseed rape in the Landsat-8 image of the same scene.

Compared to the rapeseed indices discussed in Section 2.7, the FI-R model includes the SWIR band in addition to the green, blue, red, and NIR bands. To evaluate the

Table 6 Simulated flowering index of rapeseed (FI-R) values for typical yellow features in the underlying surface

Feature[1)]	FI-R			
	Average	SD	Mean+95%CI	Mean-95%CI
Rapeseed simulation	943.16	–	958.31	927.99
Winter jasmine simulation	26.8	–	30.84	22.77
Yellow wild pansy simulation	25,671.97	–	26,318.26	25,025.69
Rapeseed pixel	25.21	245.56	26.19	24.24
Gingko pixel	1.27	0.283855	1.34	1.2
Sunflower pixel	6.41	25.36895	6.75	6.06
Yellow structure pixel	–0.1	0.912312	0.118	–0.32

[1)] The first three are the FI-R values obtained by simulating Landsat bands from measured hyperspectral data, and the last four are the FI-R values obtained from Landsat pristine pixels.

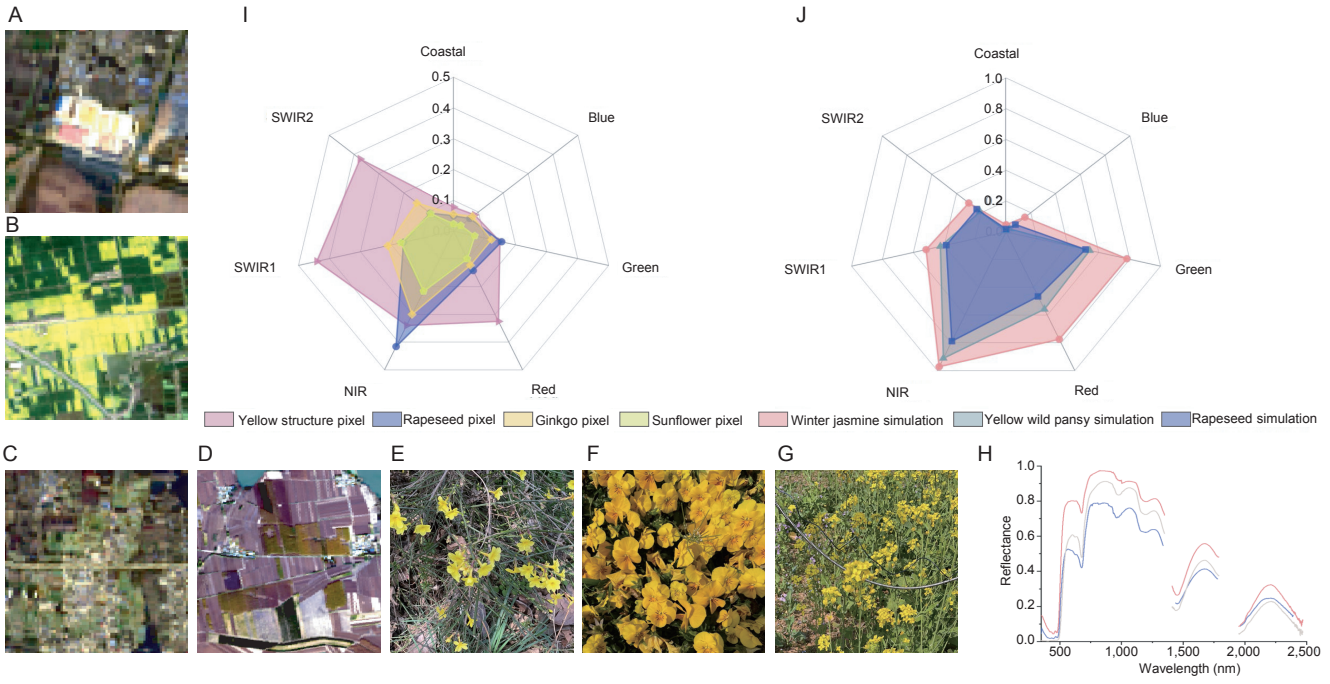


Fig. 12 Schematic diagrams of measured and simulated values for yellow features. A–D, examples of Landsat-8 image elements for yellow constructs, rapeseed in bloom, ginkgo trees during the yellow leaf period, and sunflower, respectively. E–G, spectral acquisitions of winter jasmine, yellow pansies, and rapeseed in bloom, respectively, in real time. H, hyperspectral curves of winter jasmine, yellow pansies, and rapeseed in bloom in the acquisition. I and J, Landsat-8 band value maps of yellow structures, flowering rapeseed, ginkgo trees during the yellow leaf period, sunflower and simulated Landsat-8 band value maps of winter jasmine, yellow pansies and flowering rapeseed.

improvement by including the SWIR band in extracting flowering rapeseed, we tested its impact on the FI-R model across three study areas: sites A, D, and E. The influence of the SWIR band on vegetation detection is primarily reflected in two aspects: changes in cellular water content and soil background interference (Fu *et al.* 2024a). Vegetation under stress or drought conditions exhibits greater SWIR reflectance due to cellular dehydration. In addition, the mineral composition and moisture levels in soil show significant spectral characteristics in this band. As shown in Fig. 13, when using the same threshold based on model values for pixels with low flowering intensity, the FI-R model performed well across the three study areas, despite their differences in background complexity and unit planting block size. The inclusion of the SWIR band reduced the interference from bare soil and other vegetation and improved the extraction of mixed pixels along the boundaries of rapeseed fields. These boundary pixels were more accurately identified by the FI-R model compared to models without the SWIR band. Furthermore, as shown in Table 7, the inclusion of the SWIR band notably improved the extraction accuracy for flowering rapeseed compared to models that excluded this band.

4.2. Performance of FI-R with different multispectral images

The FI-R model has good potential for applications using different multispectral images. The FI-R model was used for MODIS images of sites A, B and E and for Sentinel-2 rapeseed flowering images to test its applicability for multispectral imagery (Fig. 14). The FI-R input bands and the corresponding band wavelengths of the two multispectral sensors are shown in Table 8. Fig. 14 shows the results of rapeseed extraction at the flowering stage, and Table 9 shows the accuracy of the results. The sample dataset used to calculate the accuracy of the extraction results based on

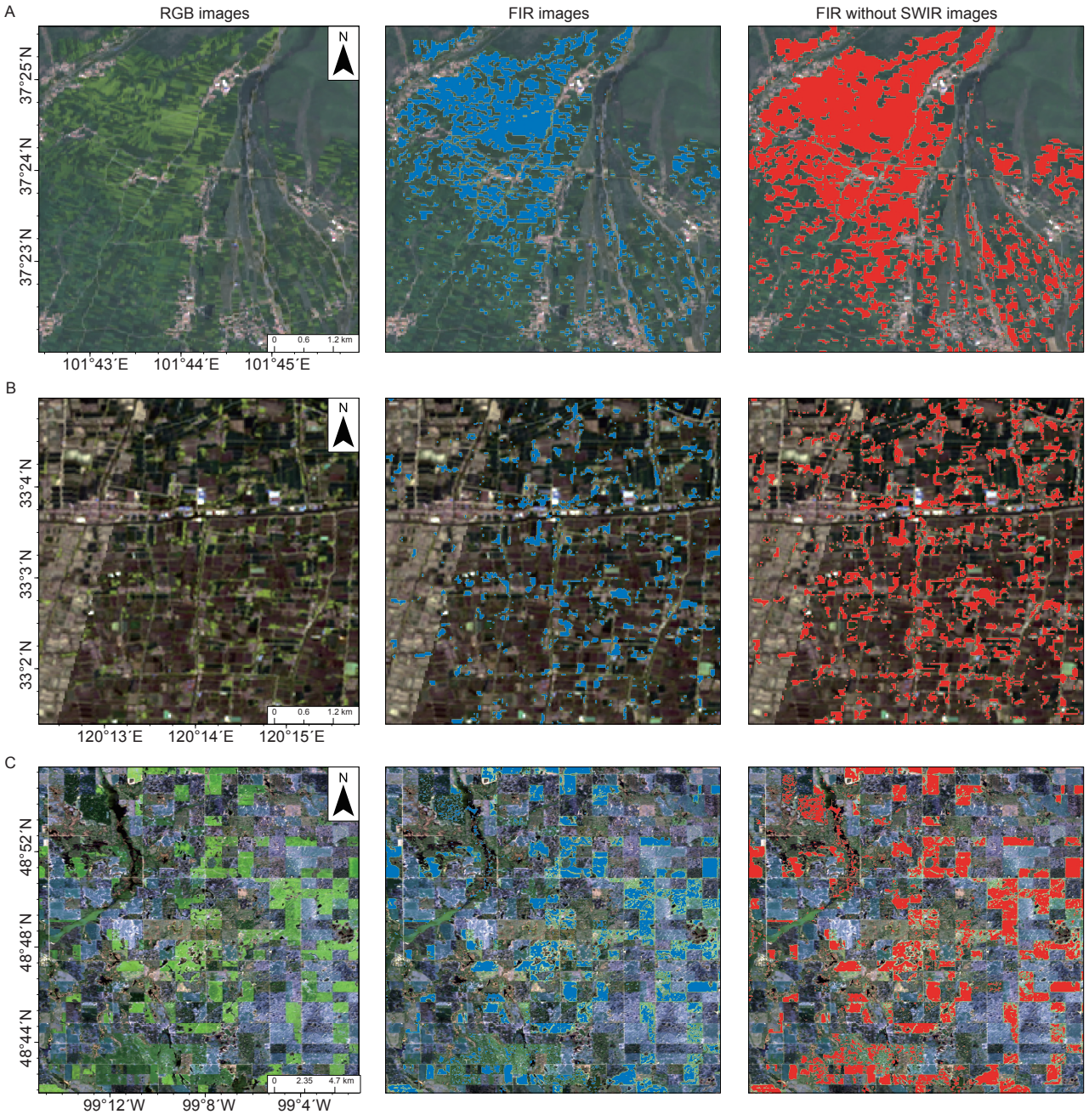


Fig. 13 Comparison of rapeseed extraction with and without the short-wave infrared (SWIR) band in the FI-R model. A–C, comparative experiments conducted in site A, site D, and site E, respectively. In the FI-R imagery, blue represents rapeseed extracted using the complete FI-R model, while red represents rapeseed extracted by the FI-R model excluding the SWIR band. The threshold for both models was determined based on the same pixel value corresponding to a rapeseed pixel with low flowering intensity.

Table 7 Accuracy validation of FI-R and the model after removing SWIR for the site A, site D and site E extraction results

Study area	Type	Overall accuracy (%)	Precision (%)	Recall (%)	F1-score (%)
Site A (Menyuan)	FI-R	97.74	92.06	97.33	94.62
	FI-R without SWIR	96.90	97.47	91.53	94.41
Site D (Taizhou)	FI-R	96.84	82.09	97.06	88.95
	FI-R without SWIR	94.29	91.79	76.24	83.30
Site E (North Dakota)	FI-R	96.21	77.48	94.80	85.87
	FI-R without SWIR	94.52	80.78	85.05	82.86

MODIS and Sentinel-2 imagery was acquired through higher resolution GF1/2 imagery.

For sites A, B, and E, the performance of the FI-R model using Sentinel-2 imagery is comparable to its performance

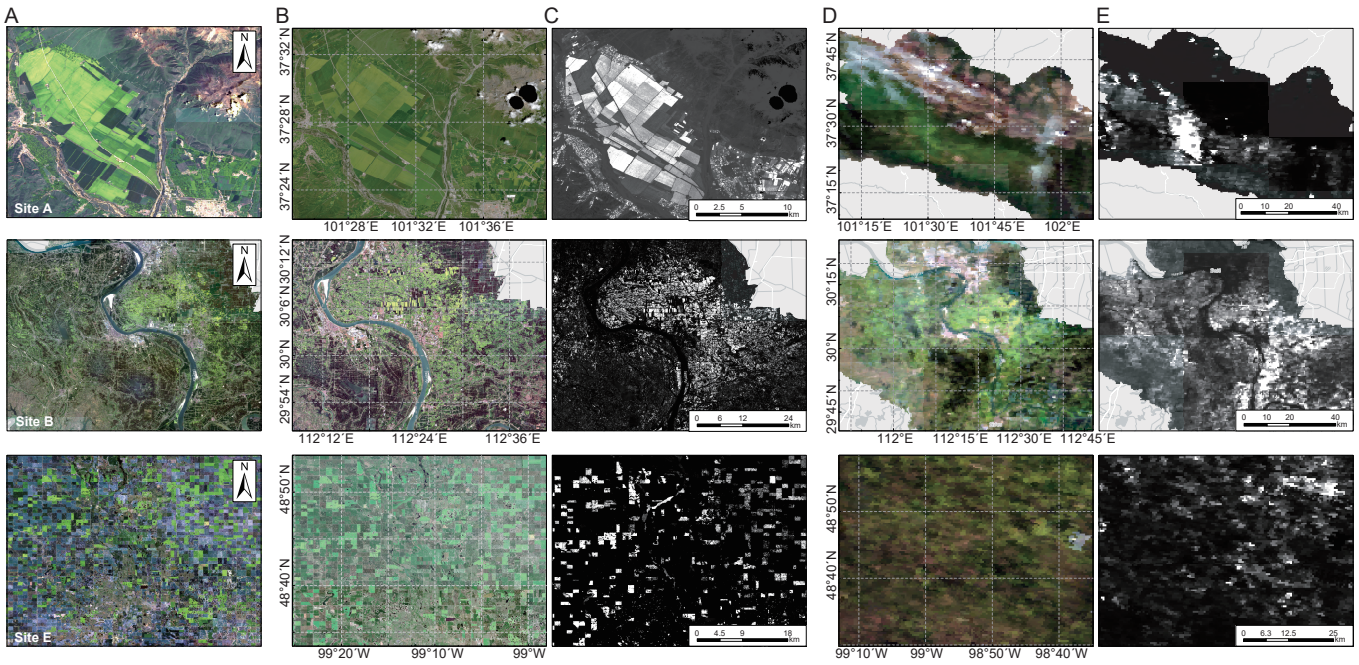


Fig. 14 Visual performance of FI-R using MODIS and Sentinel-2 images. A, Landsat-8 study area rapeseed flowering image (RGB). B and D, Sentinel-2 and MODIS flowering images (RGB) of the three study areas, respectively. C and E, visual images of rapeseed extracted by FI-R based on B and D, respectively.

Table 8 FI-R input band and corresponding band wavelengths of the MODIS and Sentinel-2 sensors

Sensor	Input band	Blue	Green	Red	NIR	SWIR1
Terra/Aqua	Band No.	B3	B4	B1	B2	B5
MODIS (MOD09GA)	Central wavelength (nm)	469	555	650	863	1,240
Sentinel-2	Band No.	B2	B3	B4	B5	B11
MSI	Central wavelength (nm) (S2A/S2B)	492.4/492.1	559.8/559.0	664.6/664.9	704.1/703.8	1,613.7/1,610.4

Table 9 Accuracy of the FI-R model rapeseed extraction results based on MODIS and Sentinel-2 imagery for three study areas

Study area	Sensor	Overall accuracy (%)	Producer's accuracy (%)	User's accuracy (%)	F1-score (%)	Precision (%)	Recall (%)
Site A (Menyuan)	MODIS	44.34	24.68	98.73	56.52	39.59	98.73
	Sentinel-2	91.61	60.15	97.35	72.75	60.48	91.26
Site B (Jingzhou)	MODIS	80.08	70.89	82.90	76.59	71.17	82.90
	Sentinel-2	88.82	71.62	93.03	80.93	93.03	71.62
Site E (North Dakota)	MODIS	70.12	53.04	64.64	58.27	53.04	64.64
	Sentinel-2	93.80	91.38	83.61	87.33	83.61	91.38

with Landsat-8 imagery, and both significantly outperform its application with MODIS imagery. The lower spatial resolution of MODIS leads to more mixed pixel issues, which presents certain challenges for the FI-R model's ability to precisely identify rapeseed. In site A, the overall accuracy with MODIS is lower, due to the sparse population and uneven distribution of rapeseed cultivation in the area. In some regions, the proportion of rapeseed to other crops within a single MODIS pixel varies significantly, and the mixed spectrum dilutes the spectral characteristics of rapeseed. At this scale, the NIR features of other vegetation are amplified, thus affecting the performance of the yellowness index in the model. In sites B and E, where rapeseed planting is more concentrated and the density of rapeseed cultivation within a MODIS pixel is higher, the FI-R model extraction results are better than in site A, with overall accuracies of 80.08 and 70.12%, respectively.

4.3. Uncertainly and improvements

The successful trial of the FI-R spectral index method for precise vegetation extraction based on the flowering stage of rapeseed demonstrates its potential for large-scale, fine-grained identification of flowering vegetation. However, if its use is extended to other flowering plants, uncertainties remain in the selection and construction of spectral features and the handling of spectrally similar phenomena. Aside from a few ornamental varieties, most cultivated rapeseed flowers are yellow. However, many other flowering plants exhibit a

wide range of flower colors, with varying pigment contents that correspond to different spectral responses, making the selection of spectral features during the flowering phase more complex.

Differences in flowering periods and durations among varieties, compounded by prolonged rainy periods in some seasons that increase cloud cover, pose significant challenges in acquiring high-quality flowering phase imagery and impact the applicability of this method over large areas. To address these issues, multi-source data fusion methods can be employed. For example, integrating microwave data such as Sentinel-1 imagery with optical images can compensate for the gaps caused by heavy cloud cover. The complex coloration of flowering plants makes avoiding the phenomenon of spectrally similar objects using a single index challenging. This issue is further complicated by the presence of mixed pixels. Although the NDVI values of flowering vegetation are reduced, the influence of flower coverage and planting density makes it difficult to determine the NDVI segmentation thresholds, which requires careful analysis for specific varieties. Higher resolution multispectral imagery can alleviate the effects of mixed pixels, while simplifying the study area background to individual farms or forest areas may reduce the occurrence of spectrally similar phenomena. Future work will focus on refining methods for the precise extraction of flowering vegetation by using the flowering phase and testing the effectiveness of this extraction method on a broader range of flowering plants.

5. Conclusion

In this study, we proposed a spectral index-based method for fine-scale vegetation extraction using flowering as a key feature. This method analyzes the ground-based hyperspectral characteristics of target vegetation and background elements, and adapts these characteristics to multispectral imagery. We developed an index model and used rapeseed as an example to construct the FI-R model. This approach enables the simple, fast, and accurate extraction of large-scale flowering rapeseed distributions under complex surface conditions using various multispectral datasets.

The FI-R index effectively enhances the separability of flowering rapeseed from other crops, and achieves rapid mapping of rapeseed over large areas with complex backgrounds. It eliminates the need for labor-intensive sample training and can be applied to various multispectral imagery platforms. Its successful application to rapeseed highlights the potential for extending this method to other types of flowering vegetation. Although this method cannot extract vegetation under cloud cover or non-flowering vegetation, it shows great potential for the fine-scale mapping of vegetation during flowering phases and for estimating interspecies yields.

Acknowledgements

This research was supported by the National Natural Science Foundation of China (42201339), and the “Science for a Better Development of Inner Mongolia” Program of the Bureau of Science and Technology of the Inner Mongolia Autonomous Region, China (2022EEDSKJXM003).

Declaration of competing interest

The authors declare that they have no conflict of interest.

Declaration of generative AI and AI-assisted technologies in scientific writing process

During the preparation of this manuscript, the authors used ChatGPT 3.5 to assist in improving the clarity and readability of the language. All content generated was carefully reviewed and revised by the authors as necessary, and the authors take full responsibility for the final content of the article.

References

Asen S. 1975. Factors affecting flower colour. *Acta Horticulturae*, **41**, 57–68.

Ashourloo D, Shahrabi H S, Azadbakht M, Aghighi H, Nematollahi H, Alimohammadi A, Matkan A A. 2019. Automatic canola mapping using time series of sentinel 2 images. *ISPRS Journal of Photogrammetry and Remote Sensing*, **156**, 63–76.

Cao Y, Li G L, Luo Y K, Pan Q, Zhang S Y. 2020. Monitoring of sugar beet growth indicators using wide-dynamic-range vegetation index (WDRVI) derived from UAV multispectral images. *Computers and Electronics in Agriculture*, **171**, 105331.

Chen B, Jin Y, Brown P. 2019. An enhanced bloom index for quantifying floral phenology using multi-scale remote sensing observations. *ISPRS Journal of Photogrammetry and Remote Sensing*, **156**, 108–120.

Chen J, Shen M, Zhu X, Tang Y. 2009. Indicator of flower status derived from in situ hyperspectral measurement in an alpine meadow on the Tibetan plateau. *Ecological Indicators*, **9**, 818–823.

Chen M, Zhang R, Jia M, Cheng L, Zhao C, Li H, Wang Z. 2024. Accurate and rapid extraction of aquatic vegetation in the china side of the Amur River Basin based on Landsat imagery. *Remote Sensing*, **16**, 654.

Cleland E, Chuine I, Menzel A, Mooney H, Schwartz M. 2007. Shifting plant phenology in response to global change. *Trends in Ecology & Evolution*, **22**, 357–365.

Freden S C, Mercanti E P, Becker M A. 1974. *Third Earth Resources Technology Satellite-1 Symposium*: *Section A–B*. *Technical Presentations*. Scientific and Technical Information Office, National Aeronautics and Space Administration, USA.

Fu B, Deng L, Sun W, He H, Li H, Wang Y, Wang Y Q. 2024a. Quantifying vegetation species functional traits along hydrologic gradients in karst wetland based on 3D mapping with UAV hyperspectral point cloud. *Remote Sensing of Environment*, **307**, 114160.

Fu B, Wu Y, Zhang S, Sun W, Jia M, Deng T, He H, Yuan B, Fan D, Wang Y. 2024b. Synergistic retrieval of mangrove vital functional traits using field hyperspectral and satellite data. *International Journal of Applied Earth Observation and Geoinformation*, **131**, 103963.

Gao L, Brian A J, Tian Q, Wang Y, Verrelst J, Mu X, Gu X, 2020. Remote sensing algorithms for estimation of fractional vegetation cover using pure vegetation index values: A review. *ISPRS Journal of Photogrammetry and Remote Sensing*, **159**, 364–377.

Gorelick N, Hancher M, Dixon M, Ilyushchenko S, Thau D, Moore R. 2017. Google earth engine: Planetary-scale geospatial analysis for everyone. *Remote Sensing of Environment*, **202**, 18–27.

Grotewold E. 2006. The genetics and biochemistry of floral pigments. *Annual Review of Plant Biology*, **57**, 761–780.

Huete A, Didan K, Miura T, Rodriguez E P, Gao X, Ferreira L G. 2002. Overview of the radiometric and biophysical performance of the MODIS vegetation indices. *Remote Sensing of Environment*, **83**, 195–213.

Ienco D, Interdonato R, Gaetano R, Ho Tong Minh D . 2019. Combining sentinel-1 and sentinel-2 satellite image time series for land cover mapping via a multi-source deep learning architecture. *ISPRS Journal of Photogrammetry and Remote Sensing*, **158**, 11–22.

Kennedy R E, Andréfouët S, Cohen W B, Gómez C, Griffiths P, Hais M, Healey S P, Helmer E H, Hostert P, Lyons M B, Meigs G W, Pflugmacher D, Phinn S R, Powell S L, Scarth P, Sen S, Schroeder T A, Schneider A, Sonnenschein R, Vogelmann J E, *et al.* 2014. Bringing an ecological view of change to Landsat-based remote sensing. *Frontiers in Ecology and the Environment*, **12**, 339–346.

Liu L, Xiao X, Qin Y, Wang J, Xu X, Hu Y, Qiao Z. 2020. Mapping cropping intensity in China using time series Landsat and Sentinel-2 images and Google Earth Engine. *Remote Sensing of Environment*, **239**, 111624.

Lyu X, Li X, Dang D, Dou H, Xuan X, Liu S, Li M, Gong J. 2020. A new method for grassland degradation monitoring by vegetation species composition using hyperspectral remote sensing. *Ecological Indicators*, **114**, 106310.

Meng S, Zhong Y, Luo C, Hu X, Wang X, Huang S. 2020. Optimal temporal window selection for winter wheat and rapeseed mapping with Sentinel-2 images: A case study of Zhongxiang in China. *Remote Sensing*, **12**, 226.

Meng Z, Song F, Huo J, Zhang M, Yang F, Zheng W, Liu C. 2023. Comparative analysis on light-temperature resource use efficiency of spring rapeseed (*Brassica napus*) differing in maturity in China Tibet under plateau climate. *Chinese Journal of Oil Crop Sciences*, **45**, 63–71. (in Chinese)

Narbona E, Del Valle J C, Arista M, Buide M L, Ortiz P L. 2021. Major flower pigments originate different colour signals to pollinators. *Frontiers in Ecology and Evolution*, **9**, 743850.

Nuijten R J G, Coops N C, Theberge D, Prescott C E. 2024. Estimation of fine-scale vegetation distribution information from RPAS-generated imagery and structure to aid restoration monitoring. *Science of Remote Sensing*, **9**, 100114.

Pandey A, Jain K, 2022. An intelligent system for crop identification and classification from UAV images using conjugated dense convolutional neural network. *Computers and Electronics in Agriculture*. **192**, 106543.

Parmesan C, Yohe G. 2003. A globally coherent fingerprint of climate change impacts across natural systems. *Nature*, **421**, 37–42.

Ribeiro A L A, Maciel G M, Siquieroli A C S, Luz J M Q, Gallis R B D A, Assis P H D S, Catão H C R M, Yada R Y. 2023. Vegetation indices for predicting the growth and harvest rate of lettuce. *Agriculture*, **13**, 1091.

Shen M, Chen J, Zhu X, Tang Y. 2009. Yellow flowers can decrease NDVI and EVI values: Evidence from a field experiment in an alpine meadow. *Canadian Journal of Remote Sensing*, **35**, 99–106.

Song Z, Zhang Z, Yang S, Ding D, Ning J. 2020. Identifying sunflower lodging based on image fusion and deep semantic segmentation with UAV remote sensing imaging. *Computers and Electronics in Agriculture*, **179**, 105812.

Sulik J J, Long D S. 2016. Spectral considerations for modeling yield of canola. *Remote Sensing of Environment*, **184**, 161–174.

Sulik J J, Long D S. 2015. Spectral indices for yellow canola flowers. *International Journal of Remote Sensing*, **36**, 2751–2765.

Sun G, Jiao Z, Zhang A, Li F, Fu H, Li Z. 2021. Hyperspectral image-based vegetation index (HSVI): A new vegetation index for urban ecological research. *International Journal of Applied Earth Observation and Geoinformation*, **103**, 102529.

Szantoi Z, Escobedo F, Abd-Elrahman A, Smith S, Pearlstine L. 2013. Analyzing fine-scale wetland composition using high resolution imagery and texture features. *International Journal of Applied Earth Observation and Geoinformation*, **23**, 204–212.

Tian H, Chen T, Li Q, Mei Q, Wang S, Yang M, Wang Y, Qin Y. 2022. A novel spectral index for automatic canola mapping by using Sentinel-2 imagery. *Remote Sensing*, **14**, 1113.

Timm B C, McGarigal K. 2012. Fine-scale remotely-sensed cover mapping of coastal dune and salt marsh ecosystems at cape cod national seashore using random forests. *Remote Sensing of Environment*, **127**, 106–117.

Vásquez R A R, Heenkenda M K, Nelson R, Segura Serrano L. 2023. Developing a new vegetation index using cyan, orange, and near infrared bands to analyze soybean growth dynamics. *Remote Sensing*, **15**, 2888.

Weiss M, Jacob F, Duveiller G. 2020. Remote sensing for agricultural applications: A meta-review. *Remote Sensing of Environment*, **236**, 111402.

Wong C Y S. 2023. Plant optics: Underlying mechanisms in remotely sensed signals for phenotyping applications. *AoB Plants*, **15**, plad039.

Wouters N, De Ketelaere B, De Baerdemaeker J, Saeys W. 2013. Hyperspectral waveband selection for automatic detection of floral pear buds. *Precision Agriculture*, **14**, 86–98.

Wu T, Li G, Yang Z, Zhang H, Lei Y, Wang N, Zhang L. 2017. Shortwave infrared imaging spectroscopy for analysis of ancient paintings. *Applied Spectroscopy*, **71**, 977–987.

Yan S, Yao X, Zhu D, Liu D, Zhang L, Yu G, Gao B, Yang J, Yun W. 2021. Large-scale crop mapping from multi-source optical satellite imageries using machine learning with discrete grids. *International Journal of Applied Earth Observation and Geoinformation*, **103**, 102485.

Yan Y, Deng L, Liu X, Zhu L. 2019. Application of UAV-based multi-angle hyperspectral remote sensing in fine vegetation classification. *Remote Sensing*, **11**, 2753.

Yang G, Huang K, Sun W, Meng X, Mao D, Ge Y. 2022. Enhanced mangrove vegetation index based on hyperspectral images for mapping mangrove. *ISPRS Journal of Photogrammetry and Remote Sensing*, **189**, 236–254.

Yao X, Yi Q, Wang F, Xu T, Zheng J, Shi Z. 2023. Estimating rice flower intensity using flower spectral information from unmanned aerial vehicle (UAV) hyperspectral images. *International Journal of Applied Earth Observation and Geoinformation*, **122**, 103415.

Yu Q, Hu Q, van Vliet J, Verburg P H, Wu W. 2018. GlobeLand30 shows little cropland area loss but greater fragmentation in China. *International Journal of Applied Earth Observation and Geoinformation*, **66**, 37–45.

Zamani-Noor N, Feistkorn D. 2022. Monitoring growth status of winter oilseed rape by NDVI and NDYI derived from UAV-Based Red–Green–Blue imagery. *Agronomy*, **12**, 2212.

Zhang B, Liu C, Wang Y, Yao X, Wang F, Wu J, King G J, Liu K. 2015. Disruption of a *CAROTENOID CLEAVAGE DIOXYGENASE 4* gene converts flower colour from white to yellow in *Brassica* species. *New Phytologist*, **206**, 1513–1526.

Zhang H, Flottmann S. 2018. Source-sink manipulations indicate seed yield in canola is limited by source availability. *European Journal of Agronomy*, **96**, 70–76.

Zhang H, Liu W, Zhang L. 2022. Seamless and automated rapeseed mapping for large cloudy regions using time-series optical satellite imagery. *ISPRS Journal of Photogrammetry and Remote Sensing*, **184**, 45–62.

Zhang Y, Wang D, Zhou Q. 2019. Advances in crop fine classification based on hyperspectral remote sensing. In: *2019 8th International Conference on Agro-Geoinformatics*. Institute of Electrical and Electronics Engineers, USA. pp. 1–6.

Zhang Z, Jin W, Dou R, Cai Z, Wei H, Wu T, Yang S, Tan M, Li Z, Wang C, Yin G, Xu B. 2023. Improved estimation of leaf area index by reducing leaf chlorophyll content and saturation effects based on red-edge bands. *IEEE Transactions on Geoscience and Remote Sensing*, **61**, 1–14.

Zheng Q, Huang W, Cui X, Shi Y, Liu L. 2018. New spectral index for detecting wheat yellow rust using Sentinel-2 multispectral imagery. *Sensors* (Basel, Switzerland), **18**, 868.

Executive Editor-in-Chief Jinshui Wu
Managing Editor Lujuan Sun